Multiscale characterization of *Caenorhabditis elegans* mutants to probe functional mechanisms of human actin pathological variants

Théo Hecquet[1,2, 3, 4], Nadine Arbogast[1,2, 3, 4], Delphine Suhner[1,2, 3, 4], Anaïs Goetz[1,2, 3, 4], Grégory Amann[1,2, 3, 4], Selin Yürekli[1,2, 3, 4], Fiona Marangoni[1,2, 3, 4], Johannes N. Greve[5], Nataliya Di Donato [6], Anne-Cécile Reymann[1,2, 3, 4]

1. Université de Strasbourg, *IGBMC UMR 7104- UMR-S 1258, F-67400 Illkirch, France*
2. CNRS*, UMR 7104, F-67400 Illkirch, France*
3. Inserm, *UMR-S 1258, F-67400 Illkirch, France*
4. *IGBMC, Institut de Génétique et de Biologie Moléculaire et Cellulaire, F-67400 Illkirch, France*
5. Institute for Biophysical Chemistry, Hannover Medical School, Fritz–Hartmann–Centre for Medical Research, 30625 Hannover, Germany
6. Department of Human Genetics, Hannover Medical School, 30§625 Hannover, Germany

Abstract

Actin plays a crucial role in diverse physiological processes via the formation of dynamic networks that determine cellular shape and mechanical properties. *De novo* variants in cytoskeletal β- and γ-actin, encoded by human *ACTB* and *ACTG1* genes, lead to a wide range of rare diseases, termed Non-Muscle Actinopathies (NMA). Variants range from missense, frameshift, truncating variants up to whole gene deletions and can induce diverse symptoms. So far, the high clinical variability and genotype-phenotype correlations in NMA remain largely unresolved. To address this question, we used CRISPR to insert in the *C. elegans* homologue *act-2* gene nine of the mutations identified in patients. Using these animal models, we performed a quantitative multiscale characterization. We uncovered a variety of perturbations: actin network defects at the micro scale, cell scale abnormalities, morphogenesis failure, as well as weaker behavioural phenotypes. Importantly, the range of developmental defects observed correlates with the severity of patients' symptoms. Thus, we provide evidence that a *C. elegans*-based approach represents a new way to investigate the mechanisms underlying NMA physiopathology or ultimately screen for therapeutic strategies.

Keywords

C. elegans, cytoplasmic actin, Non-Muscle Actinopathy, Baraitser-Winter Cerebrofrontofacial Syndrome

Introduction

The ability to dynamically assemble the actin cytoskeleton in response to internal and external triggers is a hallmark of a healthy and functional cell. Finely tuned actin architectures are coordinated to fulfil specific cellular needs and drive a multitude of cellular processes including motility, adhesion, morphogenesis, mechanotransduction, internal organisation and trafficking (Blanchoin et al. 2014; Murrell et al. 2015; Kruse et al. 2024; Lappalainen et al. 2022). Constant reorganization for adapting to external cues is intrinsically linked to the capacity of cytoskeletal actin networks to turnover and to reorganise, typically in the scale of seconds or minutes (Kruse et al. 2024). Altered cytoskeletal integrity or dynamics are implicated in many disorders ranging from hearing loss to cancer to rare developmental diseases (Parker, Baboolal, and Peckham 2020; Lai and Wong 2020). The human genome encodes six highly conserved actin isoforms, which are produced in a time- and tissue-specific manner and every actin isoform has been associated with human pathologies (Parker, Baboolal, and Peckham 2020). *De novo* missense variants, frameshift or truncating variants as well as gene deletions in the *ACTB* and *ACTG1* genes, which encode the ubiquitously expressed cytoplasmic β- and γ-actin, cause substantial cellular dysfunction and lead to a range of rare disorders, termed Non-Muscle Actinopathies (NMA) (Cuvertino et al. 2017; Latham et al. 2018; Polubothu et al. 2020; Rivière et al. 2012; Verloes et al. 2015; 1993). One particularity of this category of diseases is the broad spectrum of symptoms found in patients. NMA can range from very mild to severe neurological impairment and cortical malformations as well as reduced life expectancy of the affected patients. So far, 287 patients and 157 unique mutations have been reported to cause NMA (Donato et al. 2024). The most frequently associated NMA disease, named Baraitser-Winter cerebrofrontofacial syndrome (BWCFF), is associated with characteristic facial malformations, intellectual disability, cortical malformations, epilepsy, hearing loss and a variety of congenital anomalies (Rivière et al. 2012; Verloes et al. 2015). Even within the BWCFF subclass of NMA, a large range of symptom severity is observed.

To date, a definitive genotype-phenotype correlation within the NMA field has yet to emerge, and the functional mechanisms causing symptoms in patients remain largely elusive. It is likely that the complexity originates from both the multifaceted roles of actin and its numerous molecular partners (Actin Binding Proteins; ABP). Furthermore, the existence of compensatory mechanisms between isoforms constitute a challenge in the study of actin *in vivo* (Dugina et al. 2009; Vedula et al. 2017; Boiero Sanders et al. 2022; Michelot and Drubin 2011; Serobyan et al. 2020; Welker et al. 2023). Actin variants have been proposed to affect the cytoskeleton by four mechanisms:

insufficient availability of actin monomers, alteration of the actin filament assembly or disassembly kinetics, alteration of actin interactions with binding partners and assembly of toxic actin oligomers detrimental for proper cytoskeletal function (Greve et al. 2023). The use of purified recombinant human actin proteins allows us to quantitatively assess defects in terms of folding, thermal stability, nucleotide-binding, G- to F-actin transition and interaction with ABPs for some variants (Greve et al. 2023; 2022), validating some of these hypotheses. At the structural level, *in silico* models correlate some NMA mutations with nucleotide-binding, monomer-monomer interaction and canonical G-actin-ABP interaction surfaces (Latham et al. 2018). *In vivo*, the effects of *Actb* and *Actg1* deletions have been studied in mouse embryonic fibroblasts and in the whole animal (Patrinostro et al. 2018; Bunnell and Ervasti 2010; Bunnell et al. 2011)**.** Notably, *Actb* deletion leads to proliferation defects in mouse embryonic fibroblasts as well as embryonic lethality in mice, whereas *Actg1* null mutant mice are viable (Vanslembrouck, Ampe, and Van Hengel 2020). Currently, however, a comprehensive system capable of bridging these different scales and validating the suggested molecular to functional relationship is still missing.

To fill this gap, we chose to use the free-living nematode *Caenorhabditis elegans* (*C. elegans*) as a model to study NMA, as it provides easy access to all biologically relevant scales: from general animal fitness to stereotypical organization and development, up to cell-scale events and single molecular dynamics *in vivo*. *C. elegans* has already been used as a model for numerous diseases, notably for the study of neurodegenerative and neuromuscular disorders (Markaki and Tavernarakis 2010), thus demonstrating its capabilities in assessing the molecular to functional link in human diseases. The ease of genetic manipulation and the ability to obtain stable, isogenic strains within a matter of weeks streamlines the process of strain characterization and enables us to investigate the consequences of multiple NMA variants in a reasonable amount of time.

As is true for humans, *C. elegans* relies on different cytoplasmic actin paralogs to sustain cellular cytoskeleton integrity in all cell types. Three ubiquitously expressed actin genes (*act-1, act-2* and *act-3*) are present in a cluster and operate in a partially redundant manner, notably during early embryogenesis (Hayashi, Ono, and Ono 2019; Willis et al. 2006; S. Ono and Pruyne 2012). These three cytoplasmic *C. elegans* actins are also required for proper muscle function (S. Ono 2014). Indeed, mutants which carry some *act-2* mutations, exhibit uncoordinated adult movement or pharyngeal pumping defects (Krause et al. 1989; Landel et al. 1984; Avery 1993; Willis et al. 2006). A fourth actin-coding gene named *act-4* is expressed in different tissues, notably in neurons and in muscle cells. However, *act-4* is not as abundant or ubiquitously expressed in the early embryo as expected for an essential cytoplasmic actin such as *act-1 -2,*

and -3 (Serobyan et al. 2020). By contrast, *act-5* shows a strong tissue-specific expression in the gut and excretory cell (MacQueen et al. 2005). Among the *C. elegans* proteins, ACT-2 has the highest similarity to human cytoplasmic actin proteins, sharing 98% of amino acids with β-actin and 97% with γ-actin.

In this study, we assess the consequences of actin variants associated with BWCFF or other NMA in a model organism and present a quantitative multiscale characterization of *C. elegans* mutants. As cytoplasmic actin is required pleiotropically, we performed a global survey of mutants using well-established methods to assay both nematode fitness and specific organ function. We propose a classification of selected NMA variants with respect to the observed phenotypes in *C. elegans* and compare this classification to the severity of human patient's symptoms. This initial study of actin variants showed a strong correlation in the degree of pathological severities between *C. elegans* and humans, thus validating the use of *C. elegans* as a tool to study NMA. Importantly, this work paves the way towards the prediction of clinical severity in patients carrying novel actin variants from the outset of diagnosis.

Results

Generation of *C. elegans* models recapitulating human non-muscle actinopathies

With respects to the three *C. elegans* cytoplasmic actin genes: while *act-1* and *act-3* share identical coding sequences, they differ from *act-2* by three non-synonymous and many silent variations as well as distinct intronic regions. This allows a slightly easier CRISPR/Cas9 genome editing for *act-2* than for the others (Paix et al. 2015). In addition, similarly to its human cytoplasmic actin counterparts (*ACTB* and *ACTG1*), *C. elegans* ACT-2 is most likely present in abundant levels in all cell types. Fluorescence corresponding to the expression of a *GFP::act-2* transgene driven by an *act-2* promoter region is observed in all cells in the early embryo (20 cell stage), in the epidermis as well as in muscle cells (Willis et al. 2006). Therefore, we decided to insert a series of genetic modifications identified in the human *ACTB* and *ACTG1* genes into the *C. elegans act-2* locus. In order to span the range of severities observed in human, we chose to study an initial set of eight mutations which included mutations associated with BWCFF (*ACTB* p.L65V, *ACTB* p.G74S, *ACTB* p.G74V, *ACTB* or *ACTG1* p.T120I, *ACTB* p.R196C, *ACTB* p.R196H and *ACTG1* p.T203M) (Verloes et al. 2015; Chacon-Camacho et al. 2020; Vontell et al.

2019); as well as non-BWCFF NMA diseases (*ACTB* p.R147S and *ACTB* or *ACTG1* p.R183W) (Figure 1). Among them, p.R196 is a hot-spot identified in over 19 patients, presenting clinical variability with a high degree of brain malformation (83%, Figure 1A) (Verloes et al. 2015; Cianci et al. 2017). *ACTB* p.R147S represents a hotspot postzygotic disruption causing the mosaic skin disorders known as Becker nevus syndrome (Cai et al. 2017). This variant is likely lethal in a homozygous context (Happle 2017). *ACTB* p.R183W is associated with dystonia deafness (Eggink et al. 2017; Conboy et al. 2017; Gearing et al. 2002; Procaccio et al. 2006; Zech et al. 2017; Skogseid et al. 2018; Freitas et al. 2019).

We mapped these mutated residues on a structural model of the *C. elegans* ACT-2 monomer (G-actin) and filament to assess the localisation of the variants in different regions of the molecule that correlate with specific functions (Figure 1B). The variants are distributed across all four subdomains (SD) of the actin monomer. Two examined residues (G74, R183) are located within the nucleotide-binding cleft and, although not directly involved in nucleotide coordination or hydrolysis, contribute significantly to the release of inorganic phosphate following ATP hydrolysis (Oosterheert et al. 2023). The R147 residue is part of the target-binding cleft of the actin monomer, located between SD1 and SD3, which is lined with predominantly hydrophobic residues and represents a main interaction interface for G-actin binding proteins (Bunnell and Ervasti 2010; Dominguez and Holmes 2011). Residue T120 is part of the so-called pathogenic helix of actin (K113-T126), which constitutes a hotspot for mutations in several human actin isoforms leading to BWCFF (cytoskeletal β- and γ-actin), non-syndromic hearing loss (cytoskeletal γ-actin), thoracic aortic aneurysm (smooth muscle α-actin) and nemaline myopathy (skeletal muscle α-actin) (as reviewed in (Rubenstein and Wen 2014)). Residues R196 and T203 are both located in SD4 and are part of regions of the actin monomer that are heavily involved in the formation of monomer-monomer contacts within the actin filament. The neighbouring residue of R196, E195, forms a salt-bridge with K113 of the laterally opposing monomer. T203 is part of a threonine-rich loop that contributes to lateral and longitudinal contacts in the filament (Dominguez and Holmes 2011; Reynolds et al. 2022). Polymerization deficiencies of the p.R196H and p.T203M variant were verified in *in vitro* experiments. These three variants are predicted to impair actin capacity to polymerise into filaments *in vivo* as confirmed by *in vitro* experiments for the ACTB p.R196H T120I and T203M variants (Greve and Manstein 2024; Donato et al. 2024). The L65 residue is located in SD2 in close proximity to the DNase-loop that contributes to lateral and longitudinal interfaces and undergoes structural rearrangement upon nucleotide hydrolysis, directly affecting filament stability (Oosterheert et al. 2023; Reynolds et al. 2022).

Using these selected variants associated with various human symptoms, we generated strains harbouring each NMA mutation in the *act-2* gene, using CRISPR/Cas9 gene editing (Figure 1C, S1A). We verified that no additional mutations were present in the other four actin genes and backcrossed the strains several times before analysis. Additionally, we generated two new prospective null alleles for *act-2* (*rey016* and *rey021*) (Figure 1C), each resulting in a premature STOP codon within exon 2 (see methods section for more details). For comparison, we assayed a previously characterized *act-2* knock-out (KO) strain (allele *ok1229*) obtained via an EMS screen, which harbours a larger deletion extending beyond the 3' UTR (Willis *et al.* 2006).

ACT-2 missense variants affect the general viability of *C. elegans* to different degrees

We first compared the general viability of the different mutant *act-2* strains obtained at 20°C. We found that some mutant animals for p.R147S or p.T203M developed into homozygous adults but these few escapers produced very few embryos that were 100% lethal during embryogenesis, suggesting a fully penetrant maternal effect lethal phenotype. We thus maintained these variants as heterozygous animals using the nT1 balancer (Ferguson and Horvitz 1985). Interestingly, one mutation (p.G74V) caused lethality in heterozygous state, suggesting a dominant effect for this allele. Indeed, for this variant we obtained very few edited surviving F1 animals after CRISPR injections. Sequencing of several of these F1 transgenic animals confirmed the presence of a heterozygous G74V variant in the *act-2* gene (Figure S1B); but if some produce very few eggs, none developed into living embryos. Because we were unable to maintain a stable line expressing this variant, we did not pursue its characterization. Surprisingly, another variant affecting the same residue (p.G74S) could be maintained as homozygous. All other variants (p.L65V, p.T120I, p.R183W, p.R196C, p.R196H) as well as the KO *rey016, rey021* and *ok1229* were viable at a homozygous state and were thus maintained as such, although some of them had very few progenies. In conclusion, out of the nine single point mutation variants generated, six could be maintained as homozygous, two as heterozygous and one was inadequately viable (Figure 1D). This initial finding emphasizes the importance of these loci for development and health as well as highlights the remarkable conservation of actin across species.

act-2 gene knock-out affects reproduction and embryo viability

In order to assess how individual point variants compare with gene KO, we performed a detailed analysis of phenotypes in the absence of ACT-2 protein expression. We assessed both the newly CRISPR generated *act-2* KO strains (*rey016 and rey021* allele) as well as the EMS generated strain, *ok1229* (Willis et al. 2006). We first verified if transcriptional adaptation of another actin coding gene could compensate for the loss of *act-2*, as proposed by Willis *et al*. (Willis et al. 2006). Such a transcriptional adaptation has been reported in an *act-5* variant (Serobyan et al. 2020; Welker et al. 2023). Therefore, we measured the expression of mRNA of all actin coding genes using single animal RT-qPCR in L4 animals devoid of embryos, to avoid developmental differences in the experimental read-out (Ly, Reid, and Snell 2015). We found that both *ok1229* and *rey021* strains show a clear absence of *act-2* mRNA. By contrast, *act-1* and *act-3* expression was increased compared to wild-type (N2) animals (*act-1* fold change: *ok1229* = 2.5, *rey021* = 6.7; *act-3* fold change: *ok1229* = 4, *rey021* = 3.6), unlike *act-4* and *act-5* which only had minor fluctuations of expression (Figure 2A). We conclude that there is possibly transcriptional adaptation for actin in *C. elegans*: *act-1* and *act-3* compensate for *act-2* loss (Serobyan et al. 2020; Welker et al. 2023).

With respect to fertility and embryonic lethality, the act-2(*ok1229)* allele was described as thermosensitive, showing some limited embryonic lethality at 26°C (12/515 embryos, *ie* 2.3 % compared to WT 3/478, *ie* 0.8%) but none observed at 15°C (Willis et al. 2006). Therefore, we monitored the brood sizes and percentage of unhatched eggs of *act-2(rey021)* at different temperatures, as well as for WT and *act-2(ok1229)* animals. We observed a reduction in the number of eggs produced by the act-2(*ok1229)* and act-2(*rey021)* strains compared to the WT reference both at low and high temperatures (15°C and 25°C, Figure 2B). The *rey021* KO allele exhibited a high percentage of unhatched eggs - above 50% - for both temperatures (Figure 2B'). However, we did not detect a significant decrease in embryonic development success, in contrast with the previous description of the *act-2(ok1229)* (Figure 2B') (Willis et al. 2006). For all tested conditions we made use of Bayesian methods to infer the 95% credibility intervals of the posterior distributions of the embryonic lethality rates using our data set and both non-informative or informative priors. As showed (Figure 3B' right), intervals are clearly not separated for *act-2(rey021)* while this is not the case between the *act-2(ok1229) and WT*. Thus, these results established a difference in the developmental success of the different *act-2* KO alleles, the *act-2(ok1229)* allele showing a milder phenotype. As brood sizes and embryonic lethality were similar for the *act-2(rey021)* at both temperatures, we do not see evidence of thermosensitivity for this allele. Thus, all further experiments were performed at the standard 20°C temperature.

In order to determine if the KO allele effect was dominant or recessive, we quantified brood size and embryonic lethality from heterozygotes hermaphrodites for our two CRISPR generated strains. Overall, the progeny of *act-2* KO animals were reduced compared to WT but *rey021*/+ animals showed a higher progeny compared to *rey021*/*rey021* (Figure 2C). This effect was not observed for rey016/+ hermaphrodites, brood size being similar to that of the homozygous rey016 condition. Both progenies of heterozygous *rey021/*+ and *rey016*/+ hermaphrodites showed an embryonic viability more similar to that of the WT (Figure 2C', for this data set embryonic lethality is 16,0% for the mixed progeny of rey021/+ hermaphrodites compared to respectively 38.8% for rey021/rey021 hermaphrodites and 2.7% for WT hermaphrodites - note that a calculation of the lethality of rey021/+ embryos, representing ½ of the progeny of heterozygotes animals, lead to ~11% lethality if we do not account for additional maternal effect which could increase embryonic lethality from rey021/+ hermaphrodites). Taken together, the *act-2* KO is severely impaired both in terms of fertility and embryonic lethality, this phenotype is only partially suppressed in the heterozygous condition, such intermediate phenotype is thus pointing towards a semi-dominant also referred to as partial loss of function.

Reproductive capacity is a quantitative readout to classify actin mutants

Assessing general animal fecundity and embryonic fitness in *C. elegans* allows for the quantitative detection of potential defects in oocyte production, embryogenesis or vulva function (Schafer 2005), three actin-dependent processes. Thus, we measured the number of eggs laid and hatched by single homozygous animals expressing an *act-2* variant at 20°C. A reduction in egg laying was observed for all *act-2* variants, except for the p.G74S and p.R183W variant strains, which appeared unaffected (Figure 3A). The most severe reductions in fecundity were observed for the p.R147S and p.T203M missense variants (mean number of eggs laid: p.R147S = 2.3, p.T203M = 31.0, WT = 270.1), surpassing the reduction seen in the *act-2* KO condition (*rey021*=78) and partially rescued in the heterozygous condition (Figure S3A). All other missense variants showed a fecundity reduction less pronounced than the KO animals.

The number of unhatched eggs also varied significantly among actin variants with a trend consistent with that of fecundity (Figure 3B). The p.R147S and p.T203M variants exhibited 100% embryonic lethality if homozygous (Figure 3B) and if heterozygous, 72.7% and 58.3% respectively, thus stronger than the homozygous and heterozygous *act-2* gene KO (respectively 39.75 and 16%, Figure S3B). This indicates that a high percentage of heterozygotes p.R147S and p.T203M embryos die before hatching. The p.L65V missense variant also showed significant embryonic lethality (33.2%) although with an increased variability**.** The p.R196H variant was

affected to a significant level unlike the p.R196C variant, as showed by none overlapping 95% credibility intervals of the posterior distributions of the embryonic lethality rates calculated with Bayesian methods (Figure 3B). No other missense variants displayed a significant impairment of embryo survival. Taken together, our data suggest that p.G74S and p.R183W are not impaired in their reproductive capacity; p.R147S and p.T203M display a fully penetrant maternal-effect lethal phenotype with a likely dominant effect; while the other studied variants have much lower penetrance: a mildly decrease in fertility, associated in most cases with embryo viability comparable to WT.

Gonad internal architecture is impaired in selected mutants

As we observed an impairment in the reproductive capacity of the actin mutant strains, we investigated whether these defects were associated with abnormal organization in the *C. elegans* reproductive system. We performed a detailed analysis of gonad morphology by spinning-disk confocal microscopy using strains expressing both an actin filament probe (mex5p::Lifeact::mKate2), and endogenously labelled non-muscle myosin molecular motors (NMY-2::GFP). *C. elegans* adult hermaphrodites possess two mirror-image symmetric syncytial gonads shaped by highly organized actin structures. These structures include a connected cytoplasm-filled core, called the rachis, surrounded by germ cells with openings facing the rachis and shaped by stable actomyosin rings (Figure 3C). These rings originate from incomplete cytokinesis of primordial germ cells forming the typical specific honeycomb architecture in the functional adult gonad (Bauer et al. 2021). We first characterized the gonad morphology by measuring germ cell and rachis sizes (Figure 3D). In this analysis, the p.L65V variant presented strikingly lower values, whereas the p.T203M showed a more moderate reduction. Interestingly, the variant p.G74S presented higher rachis/gonad ratio than the control even though this is not correlated with a perturbation of fertility. Other variants had values more similar to the WT strain but exhibited greater variances. Second, we quantified defects using established criteria (Green et al. 2011) (Figure 3E). Correlated with the strong decrease of rachis size, the most pronounced phenotypes are found in the p.L65V animals, notably illustrated by the presence of 80% of degenerated gonads devoid of oocytes or early embryos. This suggests severe impairment in gonad morphogenesis and/or maintenance in these animals. Still, the penetrance was not 100% as 1 of 5 p.L65V animals harboured a normal looking gonad, which explains the viability of the strain. Other noticeable phenotypes present in animals expressing different point mutation were: the presence of 20% multinucleated oocytes in p.T203M animals as well as a 11% penetrance in

p.T120I, multinucleated germ cells in p.T203M (100%), p.T120I (33%) and p.G74V (25%). To conclude, two main phenomena can explain a reduction in brood size in actin variant genetic backgrounds: abnormal gonad internal organization; and oocyte defects likely due to DNA segregation errors, emphasizing the importance of ACT-2 in meiosis.

ACT-2 variants fail at different embryogenesis stages

We next sought to determine causes of the observed embryonic lethality. To this end, we quantified the precise stage at which embryonic lethality occurs in the actin-mutant strains (Marston and Goldstein 2006; T.K. Vuong-Brender, Yang, and Labouesse 2016) as well as eggshell shape by measuring their aspect ratios and 2D areas (Figure S3C, D). To do so, we monitored the entire duration of embryogenesis using time-lapse transmitted light video-microscopy (Figure 3F). In line with the previous embryonic lethality counts, we detected a variable proportion of *act-2* mutant embryos unable to hatch (Figure 3F). Embryonic defects were categorized into various classes: (1) in the one-cell stage, due to a failure to complete cell division (orange); (2) developmental arrest during gastrulation (yellow), a key event involving cell shape changes and migration, highly dependent on Arp2/3 actin networks (Nance 2005; Zhang, Medwig-Kinney, and Goldstein 2023); (3) developmental arrest at later steps of development (three shades of purple). Class (3) was including most cases of defects and can be further subdivided into: (3i) arrest during ventral enclosure (light purple), a process also known to rely on both protrusive and contractile actin-related events (Bernadskaya et al. 2012); (3ii) arrest during elongation, also referred to as Pat embryos (for paralyzed at two-fold, purple), suggesting muscle-defective embryos and/or defective hemidesmosomes; and (3iii) rupturing embryos during elongation, an obvious sign of impairment of tissue mechanics (dark purple) (T.K. Vuong-Brender et al. 2017). Interestingly, the total percentage of defects and their frequencies varied among the different strains but the KO condition showed a high proportion of lethality in each. In contrast, homozygous p.R147S embryos suffered severely from early embryonic death (cytokinesis and gastrulation defects) while in heterozygous p.R147S embryos, early death was reduced, and they tended to die more frequently during ventral enclosure or in later stages of elongation. As elongation requires efficient muscle contractions, this result corroborated the p.R147S impaired muscular capacity measured in the motility assay (Figure 5A, see below). The few embryos expressing the p.T203M allele, arrested at different stages of morphogenesis between gastrulation and elongation with different ratios depending on the genetic condition. These findings suggest that the p.R147S and p.T203M, both in homozygote and heterozygote embryos,

are more detrimental or toxic for early embryogenesis than the complete or partial absence of ACT-2 protein (*rey021* condition), supporting a presumptive dominant effect. To conclude, this analysis revealed variant-specific differences in the mechanisms leading to actin-related lethality, likely associated with fine-tuning of specific actin organization, dynamics or mechanoproperties at these key stages of morphogenesis.

Altered cell mechanics but surprisingly mild cortical actin disorganization in early embryos of several act-2 variants

We then asked whether defects emanate from abnormal cytoskeletal organization or impaired force production, such as abnormal cytoskeletal contractility linked to actin-myosin interaction. These possibilities are not mutually exclusive and could be linked, as architectural defects can impair contractility (Ennomani et al. 2016). We thus increased the time and scale resolution by performing spinning-disk confocal microscopy on strains carrying the LifeAct probe to follow actin filament organization as well as an endogenously labelled non-muscle myosin (NMY-2::GFP) to assess contractility during the first cell divisions of *C. elegans (Reymann et al. 2016)*.

With respect to cortical architecture and dynamics, we were surprised by the normal general organization of the actin networks observed in some *act-2* variants (Figure 4A), even though reduced polymerization capacities have been quantified biochemically using purified proteins as for p.R196H (Greve and Manstein 2024) or p.T120I and p.T203M (Donato et al. 2024). Visual inspection did not reveal major signs of impaired actin density or general organization in most embryos. For a few embryos we did observe lower density regions or holes in the cortex as for some embryos p.T203M and p.L65V (Figure 4A). Similarly, we did not detect signs of impairment in the reproducible sequence of events taking place in zygotes for most embryos. These events, which highly depend on proper cortical organization and contractility, include polarity establishment associated with cortical flows, pseudo cleavage formation, and the maintenance phase where polarity is stably maintained (Rose and Gönczy 2014; Delattre and Goehring 2021). This was evidenced by the unchanged size of the AB daughter cell in act-2 variant conditions (Figure S4). It is possible that many NMA actin variants can copolymerize with WT actin, resulting in mild phenotypes of disorganization that are still compatible with life in both humans and *C. elegans.*

Although most cells maintain seemingly normal actin cortical networks, we observed some cell-scale defects, revealing impaired cytoskeletal properties in some embryos (Figure 4B, C, D, E, F). As expected from previous analyses, we identified cell-division defects where ingression progresses smoothly but subsequently retracts (Figure 4B). This suggests that cytokinesis-ring assembly and contractility might not be impaired, but rather that failure happens at the last steps of cytokinesis completion during abscission. We also observed meiosis defects, identified by the presence of an additional nucleus present either in the AB cell or in the P0 zygote, likely due to incomplete polar body extrusion (Figure 4C). As meiosis and cytokinesis completion share common mechanical principles linked to actin, such as the formation of a contractile actin ring required to bring together closing membrane domains (Dorn et al. 2010; Flynn and McNally 2017), these failures may share a similar origin. In addition, we noticed the presence of blebs in some embryos (Figure 4D, E), note that blebs were also reported for two previously described *act-2* point mutations the *or621* and *or295* alleles (Willis et al. 2006). Blebs are transient cell protrusions that can be triggered by two main events: the detachment of the cortex from the plasma membrane or the formation of a crack in the cortex. Blebs then grow due to the internal hydrostatic pressure imposed by cortical contractility (Charras and Paluch 2008). Blebs were mostly observed at the 2-cell stage, at the interface between the AB and P1 cells before cell rounding prior to division. We observed larger blebs, mostly in p.L65V, p.T120I and p.T203M variants, emanating from AB, sometimes dragging the nucleus into the bleb, before a fast retraction period. Retraction coincided with the increase of myosin at the cortex at cytokinesis onset. Embryos presenting the blebbing phenotype also had transiently abnormal cell shapes, an overall less round, wavier cortical surface (Figure 4D) and seemingly diminished cell-cell contacts, particularly between P1 and ABp cells at the 4-cell stage. This phenotype resembles cortical blebs that were proposed to reposition the cytokinesis ring of the zygote in *ani-1(RNAi);pig-1(gm344)* embryos in the presence of excessive myosin accumulation at the anterior cortex (Pacquelet et al. 2019). While we did not observe mispositioning of the furrow or abnormal nuclei migration, the similar phenotype suggests a shared site of cortical instability.

Motility is mildly impaired for a few *act-2* variants

Like its actin cytoplasmic paralogues, ACT-2 protein is also required in muscle cells (Willis et al. 2006), evidenced by dominant mutations in *act-2* impacting *C. elegans* motility, with uncoordinated (Unc) phenotypes on 2D surfaces (Krause et al. 1989). As no such strong Unc phenotype was observed in the studied *act-2* mutants we studied, we quantified the animals'

capacity to migrate inside a pluronic gel towards a chemoattractant (food source) in a 3D burrowing assay (Lesanpezeshki et al. 2019). We observed that 82.4% of WT animals and 50.2% of mobility-deficient control animals (*unc-2*(*gk366*)) reached the food after 2 hours (Figure 5A). We detected altered 3D migration for the KO *rey021* and for the variants p.T120I, p.R183W, p.R196C, p.R196H and p.T203M, while other variants showed unaffected migration (p.L65V, p.G74S, p.R147S). We verified that these effects were not due to impaired chemosensation (Figure S5). Note that in this assay we observed an increased number of immobile animals for variants *rey021* and p.T203M only. In conclusion, six out of nine assessed *act-2* variants have impaired 3D motility, while two variants display a substantial percentage of animals that are defective both for 2D and 3D movement.

Low penetrance of neurogenesis defects

In humans, neurodevelopmental defects are the most frequent symptoms across the NMA spectrum. We thus studied neurons in *C. elegans* L4 animals. To this aim, we took advantage of a multicolour neuronal labelling transgene present in the NeuroPAL strain (Yemini et al. 2021). The NeuroPAL transgene codes for the expression of a combination of 41 neuron specific reporters for gene expression and neuronal activity, associated with four different fluorophores. This labelling allows each neuron in the animal to be identified by a unique set of fluorophores, distinguishing them from neighbouring neurons. After introducing the NeuroPAL transgene in the actin variant strains, we mapped all neurons present in the animal's midbody and tail, which include every type of neuron. For every observed animal, we did not detect altered neuronal positions. However, we did observe rare events, for each allele except p.R196H, wherein we detected the presence of a supernumerary neuron (adjacent to SDQR or in the lumbar ganglion) or a missing neuron (such as DVB or PDA, Figure 5C). These altered numbers suggest that NMA neurodevelopment defects may be reproduced in our mutant models.

Data integration to build a comparative tool

Taking advantage of the multiscale characterization performed on each mutant, our final goal was to classify the different missense variants in terms of severity. We used each of the quantitative results as variables to create a Principal Component Analysis (PCA) graphical representation (Figure 6, variables available in Figure S6). This dimension reduction allowed us to group phenotypes into different classes and allowed us to identify the few most promising

variables to be used for classification purposes (Figure S6). In the PCA plot, the WT strain was located in the left side close to the mildly affected variants (p.L65V, p.G74S, p.T120I, p.R183W, p.R196C, p.R196H), thus defining class I: characterized by negative values along dimension 1. One can note the singular position of the p.L65V, isolated in the class I group, emphasizing some specificity with respects to this variant. This result correlated with human data, where an *ACTB* p.L65V patient presented severe symptoms and early death. The KO *rey021* strain was also isolated in a more central position. Stronger phenotypes such as in p.R147S or p.T203M variants were positioned in the right half, defining class II (positive values along dimension 1). Euclidian distances calculated between each variant and the wild type reference confirmed the choice of groups: class I variants were grouped bellow a distance of 3 and class II positioned above this threshold (Figure 6B). Interestingly, heterozygous variants (*rey021*/+, p.R147S/*nT1* and p.T203M/*nT1)* were positioned closer to the WT than their homozygous counterparts, thus in accordance with a reduction of the severity of the defects in presence of one wild type *act-2* allele. Differences in the directionality of these repositioning trajectories probably underly differences in the mechanism at the origin of the defects that may affect differently the scored phenotypes (Figure S6A). To assess the robustness of our analysis we performed additional PCA either removing all the data linked to the insertion of fluorescence in the *act-2* variant genetic background thus keeping the most easily quantifiable phenotypes (Figure S6C) or removing the two most lethal strains p.R147S and p.R203M (Figure S6E). The similarity of the PCA 6B and S6C showed that the removal of these specific variables did not modify the overall positioning of strains, whereas the PCA S6E confirms the respective positioning of the homozygous variants for example, p.L65V notably clearly apart from WT and other *act-2* variant studied. In conclusion, using quantitative multiscale analysis of a panel of actin variants, we have provided access to a valuable comparative tool enabling the positioning of newly identified variants on a graded map of survival potential, if such new variants were obtained and analysed using the same parameters reflected in our PCA analysis.

Discussion

Patients affected by the rare disorders from the Non-Muscle Actinopathies (NMA) spectrum and its subclass BWCFF, exhibit a large range of symptoms and diverse survival potential, leading to complicated medical prognostics. Given the ubiquitous nature of actin, which is involved in numerous cellular events at all stages of development and throughout lifespan, it is important to

analyse multiple phenotypic parameters in animal models. Ideally in order to effectively distinguish the impact of each actin variant, these parameters should span diverse length scales: from macroscopic actin organisation to cell behaviours and phenotypes at the organism scale. In this study, we used the fast-growing and simple model organism *C. elegans* to study *in vivo* the quantitative impact of some of the associated single cytoplasmic actin variants. Using CRISPR/Cas9 genome editing, we successfully generated new *C. elegans* models expressing endogenously either *de novo* actin variants identified in human patients or premature STOP mutations to reproduce loss-of-function conditions. For each variant, we quantified general fitness, reproductive capacities, muscle-based motility, embryonic development, and neuronal differentiation. The final step using an integrated PCA analysis enabled us to summarize the phenotypic classification providing a valuable tool to position newly identified variants of unknown significance on an existing map. We believe that these data support the use of *C. elegans act-2* mutation as a pertinent and promising model for the investigation of NMA.

In the functional characterization of *act-2*, a key finding is the significant phenotypic difference between the newly generated CRISPR *act-2* knock-out strains *(rey021* and *rey016)* and the only previously reported KO strain *act-2(ok1229).* In summary for allele *act-2(rey021):* no *act-2* mRNA is detected but an upregulation of *act-1* and *act-3* mRNA levels are observed; brood sizes were reduced in rey021/rey021 condition and rey021/+ condition albeit to a lesser extent ; the progeny of rey021/+ hermaphrodites still showed 16% lethality while rey021/rey021 showed 38.8% lethality in the same assay. This *act-2(rey021)* allele thus has a semi-dominant effect as it is not fully rescued in the heterozygote condition. To conclude we suspect that this allele is haplo-insufficient, with both a maternal and zygotic effect, unlike *act-2(ok1229)* that is associated with reduced brood sizes but having comparable embryonic lethality as wild-type. We can only hypothesize the reason for the difference with *act-2(ok1229)* allele. It is possible, that a linked non-identified second-site modifier (eg. a linked suppressor mutation) was introduced during non-targeted mutagenesis, resulting in the observed differences with the CRISPR generated alleles. Similarly to human loss of a cytoplasmic actin allele that induces a compensatory transcriptional adaptation (Cuvertino et al. 2017; Bunnell et al. 2011; Tondeleir et al. 2012; Bunnell and Ervasti 2010), *C. elegans* showed transcriptional adaptation to compensate for *act-2* loss, as the closely related actin paralogue genes *act-1* and *act-3* were found to be upregulated in all KO cases. One hypothesis is that different gene compensation efficiencies are at work in the embryo but not in the L4 animals in these two genetic contexts (Welker et al. 2023; Serobyan et al. 2020). In addition to regulation via gene expression, actin levels are additionally regulated at the posttranscriptional and posttranslational levels and actin concentration was also shown to regulate actin mRNA

synthesis, all these effects are possibly differentially affecting cytoplasmic actin concentrations in these genetic contexts (Skruber, Read, and Vitriol 2018; Rodriguez and Kashina 2018). Overall, this shows that a fine tuning of the actin abundance is at work and impacting the different function we assessed, and that the presence of ACT-2 is notably important for maintaining a high fertility and ensuring the success of embryonic development.

Another significant finding was that three actin variants exhibited stronger phenotypes than the *rey021 act-2* KO, namely p.G74V, p.T203M and p.R147S. The p.G74V variant lead to an animal producing 100% lethal embryo even as a heterozygote, therefore harbours a strong dominant effect. In contrast, embryos from variants p.T203M and p.R147S are 100% lethal only when the mother is homozygous, a few embryos surviving in heterozygote condition, suggesting a fully penetrant maternal-effect lethal effect. The latter mutations were only partially improved in heterozygotes and to a much lesser extent than rey021/+ condition. Such dominant allelic effects suggest that the presence of these mutated actin proteins disrupts proper cytoskeletal function, either through essential perturbations of actin filament assembly or by interactions with actin-binding proteins. These three variants p.G74V, p.T203M and p.R147S could act as dominant negative alleles by antagonising normal polymerisation kinetics of the wild-type actin and thus affecting a diversity of cellular function notably required for the success of embryonic development. To distinguish dominant negative effect from other gain of function mechanisms, one could test if increasing amount of wild-type protein is enough to rescue the lethality. At the biochemistry level, a simplification considering actin polymerisation kinetics in isolation, such hypothesis could be easily tested using a range of protein concentrations (Greve and Manstein 2024; Greve et al. 2023). However, actin polymerisation is just one of the many parameters of actin *in vivo* role and is probably not sufficient to explain phenotypes of more complex *in vivo* situations. Indeed, if both p.R196H and p.T203M have impaired *in vitro* polymerisation rates, only p.T203M allele is severely impacting *C. elegans* fitness and embryonic success. Thus the combination of both findings *in vitro* biochemistry and *in vivo* animal models, provides key information in order to determine the impact of each actin variant.

Using these models, we observed an unexpected striking difference between two substitutions at the same locus. Animals expressing the p.G74S variant show only mild effects on embryonic viability whereas the p.G74V animals are significantly more affected, as mentioned above. This position is of particular interest because of the neighbouring His73 which is known to undergo irreversible methylation, regulating actin's interdomain flexibility in multiple species and known to affect smooth muscle contraction in mice for example (Wilkinson et al. 2019).

Additionally, due to its location within the nucleotide-binding cleft, this variant might impact the phosphate release following actin monomer incorporation into the filament. Consequently, the binding of ADF/cofilin would be perturbed, leading to impaired disassembly kinetics. Of note, *C. elegans'* ADF/cofilin homologue UNC-60 induces lethality when knocked down (K. Ono 2003). Biochemical analysis and *in vitro* studies using purified actin variants could examine these hypotheses and compare biochemically how the presence of the hydrophobic Valine is more detrimental than Serine.

Additionally and from a more fundamental perspective, characterizing actin variants is also powerful to reveal new properties of actin-networks. The observed abnormal internal gonad organization is highlighting the importance of ACT-2 for proper cytoskeleton architecture establishment in this tissue. Oocyte defects are likely due to DNA segregation errors, emphasizing the importance of ACT-2 in meiosis. Blebs, on the other hand, are intrinsically linked to cortical contractility and to cortex-to-membrane attachment, thus reinforcing the possibility that membrane-to-cortex attachment might be impaired, as suggested also by late cytokinesis defects. We use this rationale to suggest that variant p.L65V is detrimental to gonad cytoskeleton organisation and meiosis; p.R147S possibly impairs mostly branched actin networks essential at different morphogenesis stages; and p.T203M, p.T120I, and p.R196C/H impact contractility as indicated by blebbing, paralysed arrest and impaired motility. As we have demonstrated that developmental arrest at critical embryonic stages occurs at varying frequencies depending on the nature of the variant or copy number - in the case of p.R147S - we propose that these key developmental stages act as specific “barriers” to developmental success, barriers of different difficulty linked to the precise site of mutation, that must be successively overcome during embryogenesis. As developmental timings were not drastically affected (Hall, D.H., Herndon, L.A., and Altun, Z. 2017), we suspect that these barriers might have a biomechanical origin (Figure S3C). Alternatively, it is possible that some stochastic defects in the early embryo such as lineage defects or mispositioning of cells could lead to developmental arrest at later cell stages. A recent study (Xiao et al. 2022) sheds light on how cellular plasticity can buffer genetically-induced defects in *C. elegans* embryos. Thus, another hypothesis would be that our variants do not only impair morphogenesis per say - at the observed timing of arrest- but might be resulting from earlier defects which could have been initially compensated. A more detailed analysis of early embryonic development, such as using automated profiling of embryonic development (Wang et al. 2019; Green et al. 2024) or lineage tracing methods (Waliman et al. 2024) could enable to verify such hypothesis.

Observed defects commonly display incomplete penetrance and the general organization of actin at a macroscopic scale is often remarkably unaffected. This suggests an adaptation of cytoskeletal actin to perturbations, possibly originating from the cell's ability to maintain the adequate large-scale physical properties of the cortex, also known as “morphogenetic degeneracies in the actomyosin cortex” (Naganathan et al. 2018). Compensation mechanisms may ensure the robustness of embryonic development by maintaining proper cytoskeleton mechanical properties. Note that a similar robustness to cytoskeletal perturbation, in that case a resistance to microtubule disassembly, was observed in the context of *C. elegans* embryonic elongation (Priess and Hirsh 1986; Quintin et al. 2018). In our context, this could also be explained by a functional compensation by other actin isotypes expressed in early embryogenesis, notably ACT-1 or ACT-3, which might compensate for polymerization defects. *In vitro* experiments with purified proteins using mixtures of WT and mutant actin, such as p.R196H, also show a partial rescue of polymerization defects (Greve and Manstein 2024). Thus, biological variations such as gene expression fluctuation, gene compensation, actin and ABP concentrations, mechanochemical feedback or fluctuation of properties impacting cell or tissue mechanics, determine the success of embryogenesis for each individual. Consequently, each embryo may respond differently to these compensation mechanisms and might arrest at a different developmental stage. In order to go a step further, a detailed analysis of actin spatio-temporal organisation and actin molecular dynamics together with the study of some key actin binding proteins such as myosin, formin or capping-protein both in the early embryo as well as during some key stages of development, will enable to reveal additional details on the respective molecular effects of these actin variants in a living animal.

Finally, the initial investigation of the consequences of actin perturbation on neurogenesis revealed a defect in acquiring the correct number of neurons, albeit not penetrant. SDQ neurons are born from an asymmetric division followed by the death of their sister cell while DVB and PDA are born from the trans-differentiation of a rectal epithelial cell (Riva et al. 2022). Even at low penetrance, these numbers are notable, due to the 100% invariance of these neuronal lineages in *C. elegans* under wild-type conditions (Chai et al. 2022; Riva et al. 2022). These findings suggest a potential defect in the process of neuronal asymmetric division or fate acquisition, which might be amplified in the context of human cortical development where neuron numbers are far greater and asymmetric divisions have been reported in the striatum. The asymmetric divisions required for neuronal fate acquisition can depend on the asymmetry of Arp2/3 nucleated cortical actin polymerisation (Chai et al. 2022). As both actin polymerisation and Arp2/3 nucleation were already described to be impaired for some variants studied *in vitro* (Greve and Manstein 2024),

this result is not surprising and will require further investigation in *C. elegans*. Such additional studies may lead to advances in identifying the links between the molecular and functional levels that underlie NMA neuronal pathophysiology. Importantly, the NeuroPAL data using nuclei as proxy of neuronal cell positioning, did not reveal other gross defects in terms of cell migration. This might be due to the redundancy at work during development that ensures the robustness of final neuronal positioning in *C. elegans*. Assessing migration dynamics and axonal networks may uncover additional abnormalities not visible in the current analysis.

As all animal models, the use of *act-2* variants in *C. elegans* has some limitation. First of all, we do not have a confirmed correspondence between the three *C. elegans* cytoplasmic actin paralogues and the human ACTB or ACTG1 genes. Even if ubiquitous, the *act-2* expression may vary in abundance in *C. elegans* cells or tissues compared to human cytoplasmic actins, thus introducing possible bias or misinterpretations. For instance, the key role of ACT-2 for proper gonad organization and fertility might be specific to *C. elegans* and might not have a direct equivalent in human. We however think that the highly conserved *in vivo* actin-related biochemistry is ensuring, notably in the case of strong perturbation, that variants identified as inducing strong perturbation in *C. elegans* also have a negative impact in human cells.

Altogether, this work provides a new animal-model library for the study of actin variants associated with NMA. We show that different non-synonymous mutations in nematodes lead to a broad range of phenotypes as in humans, and that the severity of *C. elegans* phenotypes correlates with patients' survival potential. For example, two severely affected *C. elegans* strains are p.T147S and p.T203M. Thus correlating with the observation that several *ACTB* p.R147S patients were identified harbouring only post-zygotic mutations, thus expressed as mosaics in a subset of epithelial cells suggesting a lethality issue in human if expressed in all cells. Additionally, several patients with variant p.T203M in *ACTG1* suffer from severe BWCFF symptoms including microcephaly, profound intellectual disability and non-ambulance. This locus is in fact a hot spot for *ACTG1* but no patient with an *ACTB* mutation has been identified so far, raising the question of lethality for *ACTB* in humans. Similarly, the *C. elegans* variant p.G74V showed 100% lethality and patients with p.G74V variant in *ACTG1* are severely affected, while no *ACTB* p.G74V variant has been discovered so far. To conclude, the severity of this initial set of *C. elegans* mutants correlates with that reported in human patients.

With commercial gene editing services in *C. elegans* offering quick delivery times and automated analysis of various criteria, it is plausible that *C. elegans* NMA models be used in the future as indicators to aid clinical prognosis for humans. All the tools generated here could be

used to investigate further the mechanisms underlying NMA pathophysiology, additionally used in the context of genetic suppressor screen as well as to screen for therapeutic strategies in the future.

STAR Methods

C. elegans handling

Animals were cultured at 20°C on Nematode Growth Medium plates seeded with OP50 (Brenner 1974). Bristol strain (N2) was used as a reference. We thank the Caenorhabditis Genetics Center for providing the strains N2, DW101 and EU1383. All novel actin variants models were generated in the Reymann lab except for two alleles *act-2(syb3920)* and *act-2(syb5567)*, which were outsourced to Suny Biotech®.

C. elegans generation

We performed *dpy-10* co-CRISPR editing using purified homemade Cas9 protein, synthetic tracrRNA, and ssODN, as described in Paix et al. 2015 (Paix et al. 2015). The table of crRNA and repair template used are listed in Supplementary Table 2. Additional silent mutations were introduced either to add or remove a restriction enzyme recognition site for genotyping strategies as well as to mutate PAM or nucleotides within the sgRNA. All generated strains were then outcrossed four times with the N2 strain and all actin coding genes were sequenced to verify that only *act-2* was mutated (genotyping primers available in Supplementary Table 1). Sequencing was performed by Eurofins® and analysed using SnapGene®.

The *act-2(rey016)* allele consists of an insertion-deletion in exon 2 (33bp insertion + 816bp deletion) resulting in a frameshift and a premature STOP codon at the amino acid 70. The *act-2(rey021)* allele presents a 35bp insertion causing a frameshift and a premature STOP codon at the amino acid 120. The *act-2(ok1229)* presents a large deletion starting at the 213th amino acid and extending beyond the 3' UTR.

Note that *C. elegans* actin including ACT-2 possesses an additional cysteine after the initial methionine in the N-terminus compared to Human ACTB and ACTG1 (ACTB being MDDDIAA and ACT-2 MCDDDVAA, Figure S1A). For simplicity and easier reference to the patient's variation, we referred to the mutations' loci by omitting this additional cysteine in order to be in frame with human numbering. For example, human variation ACTB p.L65V is referred to as *act-2* p.L65V instead of *act-2* p.L66V.

Egg-laying assay

The number of eggs laid by single hermaphrodite animals was quantified on 6-well plates by isolating and transferring individual animals from well to well every 24 hours. Animals were isolated at the L4 stage. After each transfer, eggs laid were manually counted. The number of

larvae was manually counted to determine the hatching percentage 36-48 hours after the transfer. This process was repeated over the three days of the time course.

Plates were blinded by someone external to the analysis and maintained at the desired temperature (15°C, 20°C, or 25°C) throughout the experiment. Whenever we observed contamination or premature death of the P0 animal, we excluded its dataset from the analysis. Each experiment was performed on around 15 animals including a WT control group on the same medium pour.

Regarding Figure 2C, we generated heterozygote animals by crossing *act-2(rey016)* or *act-2(rey021)* animals with N2 and quantified the brood size of F1 animals. After experiment completion, we verified each animal's genotype by sequencing their progeny (genotyping primers are available in Supplementary Table 1).

3D motility assay

The ability of animals to move in a 3D medium was assessed using a pluronic-based burrowing assay as described in Lesanpezeshki et al (Lesanpezeshki et al. 2019) and optimized by Ana Carvahlo (personal communication) as follows. Liquid pluronic gel was made by adding 13g of F-127 powder into 37mL of Ultra Pure water and leaving the solution at 4°C for 48 hours. At least an hour before the experiment, pluronic gel and consumables were put at 10°C and kept refrigerated unless otherwise stated. Animals were isolated at the L4 stage 24 hours before the experiment and blinded by someone external to the experiment. Each experiment included a WT control group.

For each experiment, we put a 25µL drop of liquid pluronic gel in each well of a 24-well plate and added 10 animals into each drop. We left the plate at 20°C for a few minutes for the drop to set. Next, we added 1.3mL of liquid pluronic gel to each well to obtain a gel height of 0.6µm. After waiting 10 minutes for the gel to solidify, we added a 10µL drop of fresh concentrated (100mg/mL) OP50 to use as a chemo-attractant and kept the plate at 20°C. Then, the number of animals that reached the well's top was manually counted every 10 minutes for two hours.

The negative control, *unc-2(gk366)* is a knockout of the Human CACNA1B (calcium voltage-gated channel subunit alpha1 B) ortholog, thus predicted to enable high voltage-gated calcium channel activity expressed in whole body wall muscle and required for proper animal motility (Yemini et al. 2013).

Chemo-sensation assay

To ensure that the 3D motility defects observed were unrelated to the animals' potential inability to sense food, we performed a standard chemosensation assay. Animals, isolated at the L4 stage 24 hours before the experiment were blinded by someone external to the experiment. Animals were washed 4 times in M9 and placed at the center of a 6cm plate NGM plate without food. Fresh concentrated (100mg/mL) OP50 and Ultra Pure H20 were placed on opposite extremities of the plate. After one hour, the number of animals on each side of the plates was counted as well as the animals that did not move from their original positions ("Immobile animals" in Figure S5). The chemotaxis index was calculated using $I = \frac{n_{OP50} - n_{H_2O}}{n_{Total} - n_{immobile\ animals}}$.

RT-qPCR

Single animal RT-qPCR was performed with minimal changes from Ly, Reid and Snell (Ly, Reid, and Snell 2015). An hour before the experiment, we isolated L4 animals on a plate without food. Single L4 animals were transferred in 0.2mL Eppendorf tubes containing 2µL of lysis buffer (5 mM Tris-HCl pH 8.0, 0.5% Triton X-100, 0.5%, Tween 20, 0.25 mM EDTA and 1 mg/mL proteinase K) without the help of bacteria. Tubes were incubated at 65°C for 10 min, then at 85°C for 1min in a T100TM Thermal Cycler. After lysis completion, we used the Maxima H Minus cDNA synthesis kit. Genomic DNA was removed by adding 1µL of a master mix containing 1µL of dsDNAse buffer, 1µL of DsDNAse, and 8µL of nuclease-free water. The solution was incubated at 37°C for 2 minutes and immediately chilled on ice. cDNA synthesis was generated by adding 1µL of a mix containing 0.5µL oligo dT primer, 0.5µL 10mM dNTP, 6.5µL nuclease-free water, 2µL RT buffer, and 0.5µL Maxima H Minus enzyme mix to the lysate. We centrifuged our tubes and incubated them at 25°C for 10 minutes, then at 55°C for 30 minutes, and finally 5 minutes at 85°C. We diluted the cDNA to 25 µL with nuclease-free water and used it immediately. We prepared 6 mixes of primer (*act-1, act-2, act-3, act-4, act-5,* and *iscu-1*) containing 30.6µL of PCR grade water, 7.2µL of the forward primer at 10µM, 7.2µL of the reverse primer at 10µM (Available in Supplementary Table 1) and 90µL of the Lightcycler® 480 SYBR Green | Master mix. We added 7.5µL of primer mix for 2.5µL of lysis into a 384-well plate. We sealed the plate using the provided foil with gloves and centrifuged it at 1500xg for 2 minutes. We used a LightCycler® for qPCR following these steps; firstly a pre-incubation at 95°C for 15 minutes with a 4.4 ramp, secondly a step of amplification of 45 cycles composed of 10 seconds at 95°C with a 4.4 ramp, 15 seconds at 54°C with a 2.2 ramp and 10 seconds at 72°C with a 4.4 ramp. Thirdly, a melting curve analysis composed of 5 seconds at 95°C with a 4.4 ramp, 65 seconds at 70°C with a 2.2 ramp, and continuous heating to reach 95°C before cooling back at 40°C.

The Cts measured by the Lightcycler® were exported to a text file and were analysed using R and Rstudio (See Key resources table). Values were normalised using the Ct values of the reference gene *iscu-1* (Hoogewijs et al. 2008; Ly, Reid, and Snell 2015) and to the N2 results of the same experiment. Some animals were excluded from analysis when their Ct values exceeded 40, except in gene knockout animals. Primer pairs efficiencies were measured using standard curve analysis available in Figure S2.

Microscopy

Embryonic development time-lapse imaging

L4 animals were put on a plate at 20°C 24h before acquisition. To obtain embryos, dissections were performed on a slide covered with an Idylle® 9 well Stencell (Pasturel, Strale, and Studer 2020) with 5µL of M9 and 4 animals of the desired genotype in each well (Pasturel, Strale, and Studer 2020). Then, corpses were removed from each well using a mouth micropipette. The slide containing the dissected animals was then stuck to a #1.5 coverslip (Marienfeld Superior) and placed on a Zeiss Axio-Observer 7. DIC images were then acquired using a Hamamatsu orca flash 4.0 LT camera, every 10 seconds for 40 minutes and then every 10 minutes for at least 14 hours with a 20x/0.8 PLAN-Apochromat objective. The room temperature was controlled and set to 20-22 degrees.

Early embryogenesis

L4 animals were put on a plate at 20°C 24 hours before acquisition. Dissection of 5 animals was performed in 5µL of M9. The slide containing the dissected animals was then placed on a 2% agarose pad and placed on an inverted microscope Nikon EclipseTi-2 equipped with YOKOGAWA CSU X1 spinning disk head. Pictures were then acquired using a Photometrics Prime 95B camera each 2 or 10 second for 15 minutes with a plan apo 100x/1.45 Nikon objective.

Gonad imaging

L4 animals were immobilised in 10 µL of 1mM Levamisole and placed on a 2% agarose pad. Acquisition of gonads was performed on a LEICA DMI8 inverted microscope equipped with Yokogawa CSU W1 Spinning disk. Z-stacks were acquired using a Hamamatsu Orca Flash 4.0 camera with a 40X HCX PL APO oil immersion objective with a 0.2µm Z-step. Gonad widths were measured using FIJI by drawing a line with a 120-pixel width across the gonads germs cells and rachis in front of the +1 oocyte. Classification of phenotypes was performed visually as represented in Green et al., 2011 (Green et al. 2011). Heatmap was built using the heatmap.2

function from the R package gplots. The mean number of observed phenotypes for each variable was scaled in the row direction.

NeuroPal

L4 animals were immobilised in 7µL of 125mM sodium azide and placed on a 2% agarose pad. Acquisitions were made accordingly to https://www.hobertlab.org/wp-content/uploads/2019/09/Configuring-Your-Microscope-for-NeuroPAL-v2.pdf on a Confocal Inverted Leica TCS SP8X equipped with DMI6000 microscope White Light Laser using a 40x/1.3 HC PL APO CS oil immersion objective with a distance of 0.9µm between each Z. Mapping and comparison of the expected expression pattern is performed using the NeuroPAL software and reference atlas map.

Principal Component Analysis

Principal Component Analysis (PCA) was computed and plotted using the FactoMineR package with the PCA function using 9 dimensions, we set the 'graph' argument to true to obtain the variables factor map presented in Figure S6A. Missing values were replaced by the mean of the corresponding variable. Matrices show the quality of representation of variables across dimensions and were constructed using the get_pca_var function from the FactoMineR package. We exported the coordinates of each point and calculated the distance between each point and the WT in the two first dimensions.

In silico analysis

The primary sequence of ACT-2 from *C. elegans* was obtained from the UniProt database (ID: P10984). We used Alphafold2 (Jumper et al. 2021) to predict the structure of ACT-2 G-actin. Calculations were performed on the Halime HPC cluster at the Institute for Biophysical Chemistry at Hannover Medical School. We visualized ATP in the nucleotide binding cleft of ACT-2 G-actin by aligning the predicted ACT-2 structure with the structure of bovine ATP-bound G-actin (PDB-ID: 2BTF, (Schutt et al. 1993)). The homology model of the ACT-2 filament was generated using the SWISS-MODEL server (Waterhouse et al. 2018) with the ADP-bound human cytoskeletal β-actin filament (PDB-ID: 8DNH, (Arora et al. 2023) as a template. ChimeraX (Pettersen et al. 2021) was used for visualization of the structures and assessment of the potential implications of the variants for actin structure.

QUANTIFICATION AND STATISTICAL ANALYSIS

We used R 4.4.1 through R-Studio 2023.12.1 and JAGS for all data analysis with all the required additional packages in their latest version available. Codes are available on our lab github. The statistical analyses were performed in the frame of Bayesian and frequentist methods.

Bayesian Framework

The experimental data was enriched within the Bayesian framework by inference based on posterior distribution description. For embryonic lethality: Poisson distribution was used to estimate the embryonic lethality rates using an offset to account for the dependency with the number of eggs laid per animal (brood size) and specific parameters values for each genotype. Parameters were either given informative Normal priors: considering a very small lethality rate for WT N(0.01, 0.1), more probable lethality for all mutants N(0.1, 0.1) except the KO homozygotes for which we estimated a possible lethality of half the embryos N(0.5, 0.1). The analysis was also computed using low informative priors for all genotypes N(0,0.01) and gave similar results within a thousandth. Note that the observed 100% embryonic lethal genotypes were not included in the model. The posterior distribution was computed using the Markov chain Monte Carlo method (McMC). A burn-in of 2000 iterations, followed by 50000 iterations was used for each of the 3 McMC chains, yielding a final 28800 iterations-sample for retrieving posterior distribution characteristics. Convergence of the McMC sample chains was checked graphically. Convergence was observed in each case. For each analysis on the main outcome, we computed the 95% credible interval of the embryonic failure rates for each genotype.

Concerning the 3D motility assay, we compared the observed success rate to reach the chemoattractant after 2h by calculating their respective posterior distributions using two binomial distributions. We used the following priors: for WT mean = 0.9, sd=0.1 thus a probability modelled as p~dbeta(7.2, 0.8) and for all mutants a mean=0.5, sd=0.2 thus a probability modelled as p~dbeta(2.65, 2.65). A burn-in of 5000 iterations, followed by 105000 iterations was used for the McMC chain, in order to retrieve the posterior distributions. The odds ratio (OR), an estimation of the multiplication of the risk to fail reaching the target compared to WT, as well as the probability (p) that the difference between the two mean posterior probabilities is superior to 0.2 are indicated.

Frequentist Analysis

We used the R package rstatix for all frequentist statistical analyses. For multiple mean comparisons, we first verified the equality of variances and normality distribution of groups using

a Levene and Shapiro test respectively. If those were verified, we realized an ANOVA test followed by a Tukey's range test. Otherwise, we realized a Kruskall-Wallis followed by a Dunn test. P-values obtained with the Dunn test were adjusted using the Bonferroni method.

Statistics of Figure 5A were done on the values at the 2-hour timepoint. A summary of all tests and p-values is available in Supplementary Table 3.

Table S1. Primer sequences.

Gene	Forward	Reverse	Hybdridization temperature	Amplicon length (pb)	Purpose
act-1	ttccccacgtgttctgtg	GTTTGTGCAAGTTGACGAAG	54° C	1323	Genotyping
act-2	CTCGTAGTTGACAATGGATC	CCAACAGTGATGACTTGTCCG	56° C	776	Genotyping
act-2	gctggtttaattggaaagct	gtcagccagttcaccacgaa	55° C	2544	Genotyping
act-3	ccttcccacacccacttg	gggaccataacgatttggtg	60° C	1495	Genotyping
act-4	ctcgaccgaattctcgcc	ggttgcgggataatacgaac	50° C	1379	Genotyping
act-5	CGTTTTCTATAAACTCGACTTC	GAAATGGAAGGCACATGT	51° C	1500	Genotyping
act-1	GCCCCATCAACCATGAAG	gtttgtgcaagttgacgaag	54° C	196	RT-qPCR
act-2	CTCGTAGTTGACAATGGATC	CCTCTCTTGGATTGGGCC	54° C	226	RT-qPCR
act-3	GCCCCATCAACCATGAAG	ggtaaggcgaagagcTTAGA	54° C	183	RT-qPCR
act-4	ATCGATTGTCCACCGCAAG	ggttgcgggataatacgaac	54° C	84	RT-qPCR
act-5	GCTCCAAGCACAATGAAG	gaaatggaaggcacatgt	54° C	215	RT-qPCR
iscu-1	GAAGGTTATCGATCACTACGAG	CGTTATCGTCGACTCGAATC	54° C	137	RT-qPCR

Table S2 List of guides and repair template sequences.

Mutation and allele name	crRNA	Repair	Enzyme used for Genotyping
p.L65V, rey012	CAAUUGGGUAC UUAAGGGUA	Ggtaaattttcaaaaaattt g acc gat tgg aaa tag ttg ttt tta ggt A**TC** **GT**C ACT CTT AAA TAC CCA ATT GAG CAT GGT ATC G	BfuI
p.G74S, rey022	CGUUACCAACU GGGACGACA	CTT ACC CTT AAG TAC CCA ATT GAG CAT AGT ATC GTG ACA AAT TGG GAT GAC A**TG G**AA AAA ATC TGG CAT CAC	BsmF1
p.G74V	AGCAUGGUAUC GUUACCAAC	g ttt tta gGT ATC CTT ACC CTT AAG TAC CCA ATT GAA CAT GTT ATT GTC ACT AAC **TGG** GAC GAC ATG GAA AAA ATC TGG C	PciI
p.T120I, rey014	AUACAUGGCUG GGGUAUUGA	CT AAC CGT GAA AAG ATG ATC CAA ATC ATG TTC GAG **ACA** TTC AAT ACA CCA GCA ATG TAC GTC GCC ATC CAA GCT G	BsaBI
p.R147S, syb3920	NA.	CAA GCT GTC CTC TCC CTC TAC GCT TCC GGG TCG ACC ACG GGA ATC GTC CTC GAC TCT GGA GAT	AccI
p.R183W, syb5567	NA.	ACG CAC ACA GTC CCA ATC TAC GAA GGA TAT GCC CTC CCA CAC GCC ATC CTC CGT CTT GAC TTG GCC GGA TGG GAT CTT ACT GAT TAC CTC ATG AAG ATC CTT ACC GAG CGT GGT TAC TCT TTC ACC ACC ACC GCT GAG CGT GAA ATC GTC CGT GAC ATC AAG GAG AAG CTT TGT TAC GTC GCG	HaeIII
p.R196C, syb3909	NA.	GGA ATC GTC CTC GAC TCT GGA GAT GGT GTT ACG CAC ACA GTC CCA ATC TAC GAA GGA TAT GCC CTC CCA CAC GCC ATC CTC CGT CTT GAC TTG GCT GGA CGT GAT CTT ACT GAT TAC CTC ATG AAG ATC TTG ACC GAA TGC GGT TAC TCT TTC ACC ACC ACC GCT GAG CGT GAA ATC GTC CGT GAC ATC AAG GAG AAG CTT TGT TAC GTC GCG CTC GAT TTC GAG CAA GAA ATG GCC ACC GCC	BglII

p.R196H, rey020	AUGAAGAUCCU UACCGAGCG	CTT ACT GAT TAC CTC ATG AAA ATT CTT ACC GAG CA**T GG**T TAC TCT TTC ACC ACC ACC GCT GAG CGT GAA ATC	AIWI
p.T203M, rey023	GACGAUUUCAC GCUCAGCGG	G AAG ATC CTT ACC GAG CGT GGT TAC TCT TTC ACC **ACT** ATG GCA GAG CGA GAA ATT GTG CGT GAC ATC AAG GAG	MspAII
KO, rey021	AGCAUGGUAUC GUUACCAAC	NA.	
KO, rey016	AUACAUGGCUG GGGUAUUGA	NA.	

Legend : Lower case (non-coding), upper case (coding), red (silent mutation), blue (non-synonymous mutation of interest), bold (PAM sequence), underlined (crRNA sequence).

Table S3 : Frequentist statistics summary.

Figure 2C, Kruskall-Wallis and Dunn test with adjusted p-value.					
	WT	*rey021/rey021*	*rey021/+*	*rey016/rey016*	*rey016/+*
WT		2.45e-10	3.92e-2	1.16e-4	9.14e-5
rey021/rey021			1.03e-1	7.83e-1	

Figure 2C', Kruskall-Wallis and Dunn test with adjusted p-value and extreme outliers.					
	WT	*rey021/rey021*	*rey021/+*	*rey016/rey016*	*rey016/+*
WT		4.40e-9	9.36e-1	9.58e-5	9.07e-1
rey021/rey021			1.07e-2	1	

Figure 2C', Kruskall-Wallis and Dunn test with adjusted p-value and no extreme outliers.					
	WT	*rey021/rey021*	*rey021/+*	*rey016/rey016*	*rey016/+*
WT		4.98e-10	1	1.12e-5	2.58e-1
rey021/rey021			3.61e-3	1	

Figure 3A, Kruskall-Wallis and Dunn test with adjusted p-value.

	WT	*rey021*
rey021	4.29e-6	
p.L65V	1.02e-1	1
p.G74S	1	3.99e-2
p.T120I	1.84e-2	1
p.R147S	1.62e-10	1
p.R183W	1	3.56e-2
p.R196C	1	4.23e-1
p.R196H	1	4.01e-1
p.T203M	2.39e-7	1

Figure 3B, Kruskall-Wallis and Dunn test with adjusted p-value and extreme outliers.

	WT	*rey021*
rey021	1.49e-5	
p.L65V	1.07e-2	1
p.G74S	1	2.35e-1
p.T120I	1	5.84e-3
p.R147S	2.01e-4	1
p.R183W	1	8.08e-3
p.R196C	1	1.18e-1
p.R196H	1	3.43e-1
p.T203M	1.76e-7	1

Figure 3B, Kruskall-Wallis and Dunn test with adjusted p-value and no extreme outliers.

	WT	*rey021*
rey021	3.60e-6	
p.L65V	1.15e-2	1
p.G74S	1	3.11e-1
p.T120I	1	5.99e-3
p.R147S	7.34e-5	1
p.R183W	1	2.93e-3
p.R196C	1	2.50e-1
p.R196H	1	4.69e-1
p.T203M	4.25e-8	1

Figure 3D, ANOVA and Tukey_hsd with adjusted p-value and extreme outliers.						
	p.L65V	p.G74S	p.T120I	p.R196C	p.R196H	p.T203M
WT	3.03e-2	2.02e-1	1	9.91e-1	8.54e-1	3.07e-1

Figure 3D, Kruskall-Wallis and Dunn test with adjusted p-value and no extreme outliers.						
	p.L65V	p.G74S	p.T120I	p.R196C	p.R196H	p.T203M
WT	2.60e-1	3.93e-1	1	1	1	1

Figure S3A, Kruskall-Wallis and Dunn test with adjusted p-value.			
	rey021/+	p.R147S/*nT1*	p.T203M/*nT1*
WT	2.12e-4	4.90e-3	3.68e-2

Figure S3B, Kruskall-Wallis and Dunn test with adjusted p-value and extreme outliers.			
	rey021/+	p.R147S/nT1	p.T203M/nT1
WT	9.50e-1	7.74e-5	1.12e-2

Figure S3B, Kruskall-Wallis and Dunn test with adjusted p-value and no extreme outliers.			
	rey021/+	p.R147S/*nT1*	p.T203M/*nT1*
WT	1	4.45e-6	1.20e-3

Figure 5A Kruskall-Wallis and Dunn test with adjusted p-value and extreme outliers.		
	WT	*unc-2*(*gk366*)
unc-2(*gk366*)	6.67e-3	
rey021	5.69e-2	1
p.L65V	1	7.67e-3
p.G74S	1	1
p.T120I	4.25e-2	1
p.R147S	1	1
p.R183W	9.14e-1	1
p.R196C	1.66e-1	1
p.R196H	1.52e-3	1

p.T203M	9.15e-1	1

Key Resources Table

REAGENT or RESOURCE	SOURCE	IDENTIFIER
Restriction enzyme: BfuI	Thermo Fisher Scientific	ER1501
Restriction enzyme: BsmF1	New England Biolabs	R0572L
Restriction enzyme: PciI	New England Biolabs	R0655L
Restriction enzyme: BsaBI	Thermo Fisher Scientific	ER1711
Restriction enzyme: AccI	New England Biolabs	R0161L
Restriction enzyme: HaeIII	New England Biolabs	R018L
Restriction enzyme: BglII	New England Biolabs	R0144L
Restriction enzyme: AlwI	New England Biolabs	R0513S
Restriction enzyme: MspA1I	New England Biolabs	R0577S
Cas9	homemade	
F-127	Sigma-Aldrich	P2443 ; CAS: 9003-11-6
5 mM Tris-HCl pH 8.0	Euromedex	EU0011
Triton X-100	Sigma-Aldrich	93418
Tween 20	Sigma-Aldrich	P2287
EDTA	Euromedex	EU0007
1 mg/mL proteinase K	Thermo Fisher Scientific	EO0491
Levamisole	Eurobio Scientific	SP-5000-18
Sodium Azide	Interchimsa	NJK63A
Critical commercial assays		
Maxima H Minus First Strand cDNA Synthesis Kit	Thermo Fisher Scientific	K1651
Lightcycler® 480 SYBR Green | Master mix	Roche Life Science	04887352001
Experimental models: Organisms/strains		
C. elegans: Strain ACR061: act-2 (rey012 [Leu65Val]) V	This paper	N/A
C. elegans: Strain ACR096: nmy-2(cp7[nmy-2::gfp + LoxP unc-119(+) LoxP]) I; gesIs001 ([mex-5p::Lifeact::mKate::nmy-2UTR, unc-119 (+)]) ; unc119(ed3) III; act-2 (rey012 [Leu65Val]) V	This paper	N/A

C. elegans: Strain ACR153: otIs696 ; act-2 (rey012 [Leu65Val]) V	This paper	N/A
C. elegans: Strain ACR108: act-2 (rey022 [Gly74Ser]) V	This paper	N/A
C. elegans: Strain ACR224: nmy-2(cp7[nmy-2::gfp + LoxP unc-119(+) LoxP]) I; gesIs001 ([mex-5p::Lifeact::mKate::nmy-2UTR, unc-119 (+)]) ; unc119(ed3) III; act-2 (rey022 [Gly74Ser]) V	This paper	N/A
C. elegans: Strain ACR165: otIs696 ; act-2 (rey022 [Gly74Ser]) V	This paper	N/A
C. elegans: Strain ACR070: act-2 (rey014 [Thr120Ile]) V	This paper	N/A
C. elegans: Strain ACR139: nmy-2(cp7[nmy-2::gfp + LoxP unc-119(+) LoxP]) I; gesIs001 ([mex-5p::Lifeact::mKate::nmy-2UTR, unc-119 (+)]) ; unc119(ed3) III; act-2 (rey014 [Thr120Ile]) V	This paper	N/A
C. elegans: Strain ACR137: otIs696 ; act-2 (rey014 [Thr120Ile]) V	This paper	N/A
C. elegans: Strain ACR168: act-2(syb3920[Arg147Ser]/nT1[qIs51]) V	This paper	N/A
C. elegans: Strain ACR216: otIs696 ; act-2(syb3920[Arg147Ser]/nT1[qIs51]) V	This paper	N/A
C. elegans: Strain PHX5567: act-2 (syb5567 [Arg183Thr]) V	This paper	N/A
C. elegans: Strain ACR125: act-2 (syb3909[Arg196Cys]) V	This paper	N/A
C. elegans: Strain ACR135: nmy-2(cp7[nmy-2::gfp + LoxP unc-119(+) LoxP]) I; gesIs001 ([mex-5p::Lifeact::mKate::nmy-2UTR, unc-119 (+)]) ; unc119(ed3) III; act-2 (syb3909[Arg196Cys]) V	This paper	N/A
C. elegans: Strain ACR166: otIs696 ; act-2 (syb3909[Arg196Cys]) V	This paper	N/A
C. elegans: Strain ACR085: act-2 (rey020 [Arg196His]) V	This paper	N/A
C. elegans: Strain ACR107: nmy-2(cp7[nmy-2::gfp + LoxP unc-119(+) LoxP]) I; gesIs001 ([mex-5p::Lifeact::mKate::nmy-2UTR, unc-119 (+)]) ; unc119(ed3) III; act-2 (rey020 [Arg196His]) V V	This paper	N/A
C. elegans: Strain ACR136: otIs696 ; act-2(rey020[Arg196His]) V	This paper	N/A
C. elegans: Strain ACR099: act-2(rey023[Thr203Met]) / DnT1[qIs50] (IV;V)	This paper	N/A
C. elegans: Strain ACR122: gesIs001 ([mex-5p::Lifeact::mKate::nmy-2UTR, unc-119 (+)]) ; unc119(ed3) III; act-2(rey023 [Thr203Met]) / DnT1[qIs50] (IV;V)	This paper	N/A
C. elegans: Strain ACR219: otIs696 ; act-2(rey023[Thr203Met]) / DnT1[qIs50] (IV;V)	This paper	N/A

C. elegans: Strain EU1383: act-2(ok1229) V	(Willis et al. 2006)	WB Strain: EU1383; WormBase: WBStrain00007359
C. elegans: Strain ACR162: act-2(ok1229) V	This paper	N/A
C. elegans: Strain ACR161: act-2 (rey016(KO)) V	This paper	N/A
C. elegans: Strain ACR149: act-2 (rey021(KO)) V	This paper	N/A
C. elegans: Strain ACR173: otIs696 ; act-2(rey021[KO]) V	This paper	N/A
C. elegans: Strain DW101: atl-1(tm853) V/ DnT1[qIs50] (IV;V)	S. Mitani	WB Strain: DW101; WormBase: WBStrain00006438
C. elegans: Strain VC854: unc-2(gk366) X	The C. elegans Deletion Mutant Consortium, 2012	WB Strain: VC854; WormBase: WBStrain00036122
C. elegans: Strain SWG007: nmy-2(cp7[nmy-2::gfp + LoxP unc-119(+) LoxP]) I; gesIs001 ([mex-5p::Lifeact::mKate::nmy-2UTR, unc-119 (+)]) ; unc119(ed3) III	(Reymann et al. 2016)	
C. elegans: Strain OH15495: otIs696	(Yemini et al. 2021)	WB Strain: OH15495; WormBase: WBStrain00047403
C. elegans: Strain N2	Brenner, 1974	WB Strain: N2; WormBase: WBStrain00000001
Oligonucleotides		
Primers for Genotyping	See Table S1	N/A
Primers for RT-qPCR	See Table S1	N/A
Recombinant DNA		
CRISPR guides and repair templates	See Table S2	IDT
Software and algorithms		
ImageJ		https://imagej.nih.gov/ij/
NeuroPAL	(Yemini et al. 2021)	NeuroPAL — Yemini Lab
SnapGene		

R 4.4.1	The R Project for Statistical Computing	Index of /bin/windows/base/old/4.4.1
R-Studio 2023.12.1	RStudio Integrated Development Environment	2023.12.1+402.pro1
JAGS 4.3.2.	Just Another Gibbs Sampler	JAGS - Just Another Gibbs Sampler
Other		
Idylle® 9 well Stencell	(Pasturel, Strale, and Studer 2020)	

Acknowledgments

We would like to particularly thank the Imaging Center of IGBMC (ici.igbmc.fr) with the assistance of Elvire Guiot, Erwan Grandgirard, Yves Lutz and Bertrand Vernay. We warmly thank Dietmar Manstein (D.J.M) for his significant contributions to the project design and throughout grant application procedures. We also thank Juliette Godin, Sophie Quintin, Michel Labouesse and Patrick Reilly for critical reading of the manuscript. Thanks to Robert W. Fernandez post doc from Oliver Hobert's lab for training us to NeuroPAL as well as to our junior visitor scientists Fanny Bouvier, Emil Zessin and Johann Marois for their help.

Funding

This work was funded by European Joint Program for Rare Diseases through the European Union's Horizon 2020 research and innovation program under the EJP RD COFUND–EJP N° 825575. N.D.D. and D.J.M./J.N.G. with support from the German Federal Ministry of Education and Research under Grant Agreements 01GM1922A and 01GM1922B, respectively. A-C.R. under the project ANR-19-RAR4-0001-03. A-C.R. was also supported by the French Fondation Maladies Rares under the project SAM-2022-121409. This work of the Interdisciplinary Thematic Institute IMCBio+, as part of the ITI 2021-2028 program of the University of Strasbourg, CNRS and Inserm, was supported by IdEx Unistra (ANR-10-IDEX-0002), and by SFRI-STRAT'US project (ANR-20-SFRI-0012) and EUR IMCBio (ANR-17-EURE-0023) under the framework of the France 2030 Program. N.D.D received grant support from Deutsche Forschungsgemeischaft (DFG) (DI 2170/3-1 and DI 2170/5-1), Else-Kröner-Fresenius Stiftung (2020_EKES.04) and German Federal Ministry of Education and Research under Grant Agreements 01GM1922A. We acknowledge the Imaging Center of IGBMC, member of the national infrastructure France-BioImaging supported by the French National Research Agency (ANR-10-INBS-04). A-C.R. is a CNRS investigator. N.A. is an Unistra technician personnel. J.N.G. is supported by the HiLF I grant for early career researchers from Hannover Medical School. Some strains were also provided by the CGC, which is funded by NIH Office of Research Infrastructure Programs (P40 OD010440).

Authors contribution

Conceptualisation A-C.R., N.D.D., T.H.; Methodology A-C.R., T.H.; Investigation, A-C.R., T.H., N.A., A.G. S.Y., F.M., J.G.; Writing -Original Draft, A-C.R., T.H.; Writing -Review & Editing, A-C.R., T.H., J.G., N.D.D.; Funding Acquisition, A-C.R., N.D.D, D.J.M, J.G.; Resources, A-C.R.; Supervision, A-C.R..

"The authors declare no competing interest."

References

Arora, Amandeep S, Hsiang-Ling Huang, Ramanpreet Singh, Yoshie Narui, Andrejus Suchenko, Tomoyuki Hatano, Sarah M Heissler, Mohan K Balasubramanian, and Krishna Chinthalapudi. 2023. "Structural Insights into Actin Isoforms." Edited by Pekka Lappalainen, Anna Akhmanova, and Vitold Galkin. *eLife* 12 (February):e82015. https://doi.org/10.7554/eLife.82015.

Avery, L. 1993. "The Genetics of Feeding in Caenorhabditis Elegans." *Genetics* 133 (4): 897–917. https://doi.org/10.1093/genetics/133.4.897.

Bauer, Jack, Vincent Poupart, Eugénie Goupil, Ken C. Q. Nguyen, David H. Hall, and Jean-Claude Labbé. 2021. "The Initial Expansion of the C. Elegans Syncytial Germ Line Is Coupled to Incomplete Primordial Germ Cell Cytokinesis." *Development (Cambridge, England)* 148 (18): dev199633. https://doi.org/10.1242/dev.199633.

Bernadskaya, Yelena Y, Andre Wallace, Jillian Nguyen, William A Mohler, and Martha C Soto. 2012. "UNC-40/DCC, SAX-3/Robo, and VAB-1/Eph Polarize F-Actin during Embryonic Morphogenesis by Regulating the WAVE/SCAR Actin Nucleation Complex." Edited by Andrew D Chisholm. *PLoS Genetics* 8 (8): e1002863. https://doi.org/10.1371/journal.pgen.1002863.s003.

Blanchoin, Laurent, Rajaa Boujemaa-Paterski, Cécile Sykes, and Julie Plastino. 2014. "Actin Dynamics, Architecture, and Mechanics in Cell Motility." *Physiological Reviews* 94 (1): 235–63. https://doi.org/10.1152/physrev.00018.2013.

Boiero Sanders, Micaela, Christopher P Toret, Audrey Guillotin, Adrien Antkowiak, Thomas Vannier, Robert C Robinson, and Alphée Michelot. 2022. "Specialization of Actin Isoforms Derived from the Loss of Key Interactions with Regulatory Factors." *The EMBO Journal* 41 (5): e107982. https://doi.org/10.15252/embj.2021107982.

Bunnell, Tina M., Brandon J. Burbach, Yoji Shimizu, and James M. Ervasti. 2011. "β-Actin Specifically Controls Cell Growth, Migration, and the G-Actin Pool." *Molecular Biology of the Cell* 22 (21): 4047–58. https://doi.org/10.1091/mbc.e11-06-0582.

Bunnell, Tina M., and James M. Ervasti. 2010. "Delayed Embryonic Development and Impaired Cell Growth and Survival in *Actg1* Null Mice." *Cytoskeleton* 67 (9): 564–72. https://doi.org/10.1002/cm.20467.

Cai, Emily D., Bryan K. Sun, Audris Chiang, Anna Rogers, Laura Bernet, Binbin Cheng, Joyce Teng, Kerri E. Rieger, and Kavita Y. Sarin. 2017. "Postzygotic Mutations in Beta-Actin Are Associated with Becker's Nevus and Becker's Nevus Syndrome." *The Journal of Investigative Dermatology* 137 (8): 1795–98. https://doi.org/10.1016/j.jid.2017.03.017.

Chacon-Camacho, Oscar F., Tania Barragán-Arévalo, Camilo E. Villarroel, Mónica Almanza-Monterrubio, and Juan Carlos Zenteno. 2020. "Previously Undescribed Phenotypic Findings and Novel *ACTG1* Gene Pathogenic Variants in Baraitser-Winter Cerebrofrontofacial Syndrome." *European Journal of Medical Genetics* 63 (5): 103877. https://doi.org/10.1016/j.ejmg.2020.103877.

Chai, Yongping, Dong Tian, Zhiwen Zhu, Yuxiang Jiang, Shanjin Huang, Dou Wu, Guangshuo Ou, and Wei Li. 2022. "Wnt Signaling Polarizes Cortical Actin Polymerization to Increase Daughter Cell Asymmetry." *Cell Discovery* 8 (1): 22. https://doi.org/10.1038/s41421-022-00376-4.

Charras, Guillaume, and Ewa Paluch. 2008. "Blebs Lead the Way: How to Migrate without Lamellipodia." *Nature Reviews. Molecular Cell Biology* 9 (9): 730–36. https://doi.org/10.1038/nrm2453.

Cianci, Paola, Grazia Fazio, Sara Casagranda, Marco Spinelli, Carmelo Rizzari, Gianni Cazzaniga, and Angelo Selicorni. 2017. "Acute Myeloid Leukemia in Baraitser–Winter Cerebrofrontofacial

Syndrome." *American Journal of Medical Genetics Part A* 173 (2): 546–49. https://doi.org/10.1002/ajmg.a.38057.

Conboy, Erin, Filippo Vairo, Darrel Waggoner, Carole Ober, Soma Das, Radhika Dhamija, Eric W. Klee, and Pavel Pichurin. 2017. "Pathogenic Variant in ACTB, p.Arg183Trp, Causes Juvenile-Onset Dystonia, Hearing Loss, and Developmental Delay without Midline Malformation." *Case Reports in Genetics* 2017:9184265. https://doi.org/10.1155/2017/9184265.

Cuvertino, Sara, Helen M Stuart, Kate E Chandler, Neil A Roberts, Ruth Armstrong, Laura Bernardini, Sanjeev Bhaskar, et al. 2017. "ACTB Loss-of-Function Mutations Result in a Pleiotropic Developmental Disorder." *The American Journal of Human Genetics* 101 (6): 1021–33.

Delattre, Marie, and Nathan W. Goehring. 2021. "The First Steps in the Life of a Worm: Themes and Variations in Asymmetric Division in C. Elegans and Other Nematodes." *Current Topics in Developmental Biology* 144:269–308. https://doi.org/10.1016/bs.ctdb.2020.12.006.

Dominguez, Roberto, and Kenneth C. Holmes. 2011. "Actin Structure and Function." *Annual Review of Biophysics* 40 (Volume 40, 2011): 169–86. https://doi.org/10.1146/annurev-biophys-042910-155359.

Donato, Nataliya Di, N. M. A. Consortium, Andrew Thom, Andreas Rump, Johannes N. Greve, Marcus Kropp, Juan Cadiñanos, et al. 2024. "Genomic and Biological Panoramas of Non-Muscle Actinopathies." medRxiv. https://doi.org/10.1101/2024.08.21.24310320.

Dorn, Jonas F, Li Zhang, Véronique Paradis, Daniel Edoh-Bedi, Sylvester Jusu, Paul S Maddox, and Amy Shaub Maddox. 2010. "Actomyosin Tube Formation in Polar Body Cytokinesis Requires Anillin in C. Elegans." *Current Biology* 20 (22): 2046–51.

Dugina, Vera, Ingrid Zwaenepoel, Giulio Gabbiani, Sophie Clément, and Christine Chaponnier. 2009. "β- and γ-Cytoplasmic Actins Display Distinct Distribution and Functional Diversity." *Journal of Cell Science* 122 (16): 2980–88. https://doi.org/10.1242/jcs.041970.

Eggink, Hendriekje, Martje E. van Egmond, Corien C. Verschuuren-Bemelmans, Marleen C. Schönherr, Tom J. de Koning, D.L. Marinus Oterdoom, J. Marc C. van Dijk, and Marina A.J. Tijssen. 2017. "Dystonia-Deafness Syndrome Caused by a β-Actin Gene Mutation and Response to Deep Brain Stimulation." *Movement Disorders* 32 (1): 162–65. https://doi.org/10.1002/mds.26842.

Ennomani, Hajer, Gaëlle Letort, Christophe Guérin, Jean-Louis Martiel, Wenxiang Cao, François Nédélec, Enrique M De La Cruz, Manuel Théry, and Laurent Blanchoin. 2016. "Architecture and Connectivity Govern Actin Network Contractility." *Current Biology*, February, 1–12.

Ferguson, E. L., and H. R. Horvitz. 1985. "Identification and Characterization of 22 Genes That Affect the Vulval Cell Lineages of the Nematode Caenorhabditis Elegans." *Genetics* 110 (1): 17–72. https://doi.org/10.1093/genetics/110.1.17.

Flynn, Jonathan R., and Francis J. McNally. 2017. "A Casein Kinase 1 Prevents Expulsion of the Oocyte Meiotic Spindle into a Polar Body by Regulating Cortical Contractility." *Molecular Biology of the Cell* 28 (18): 2410–19. https://doi.org/10.1091/mbc.e17-01-0056.

Freitas, Julian Letícia, Thiago Cardoso Vale, Orlando G.P. Barsottini, and José Luiz Pedroso. 2019. "Expanding the Phenotype of Dystonia-Deafness Syndrome Caused by ACTB Gene Mutation." *Movement Disorders Clinical Practice* 7 (1): 86–87. https://doi.org/10.1002/mdc3.12854.

Gearing, Marla, Jorge L. Juncos, Vincent Procaccio, Claire-Anne Gutekunst, Elaine M. Marino-Rodriguez, Kymberly A. Gyure, Shoichiro Ono, et al. 2002. "Aggregation of Actin and Cofilin in Identical Twins with Juvenile-Onset Dystonia." *Annals of Neurology* 52 (4): 465–76. https://doi.org/10.1002/ana.10319.

Green, Rebecca A., Huey-Ling Kao, Anjon Audhya, Swathi Arur, Jonathan R. Mayers, Heidi N. Fridolfsson, Monty Schulman, et al. 2011. "A High-Resolution C. Elegans Essential Gene Network Based on Phenotypic Profiling of a Complex Tissue." *Cell* 145 (3): 470–82. https://doi.org/10.1016/j.cell.2011.03.037.

Green, Rebecca A., Renat N. Khaliullin, Zhiling Zhao, Stacy D. Ochoa, Jeffrey M. Hendel, Tiffany-Lynn Chow, HongKee Moon, Ronald J. Biggs, Arshad Desai, and Karen Oegema. 2024. "Automated Profiling of Gene Function during Embryonic Development." *Cell* 187 (12): 3141-3160.e23. https://doi.org/10.1016/j.cell.2024.04.012.

Greve, Johannes N., and Dietmar J. Manstein. 2024. "Baraitser–Winter Syndrome Hotspot Mutation R196H in Cytoskeletal β–Actin Reduces F–Actin Stability and Perturbs Interaction with the Arp2/3 Complex." https://doi.org/10.1101/2024.03.20.585892.

Greve, Johannes N., Anja Marquardt, Robin Heiringhoff, Theresia Reindl, Claudia Thiel, Nataliya Di Donato, Manuel H. Taft, and Dietmar J. Manstein. 2023. "The Non–Muscle Actinopathy–Associated Mutation E334Q in Cytoskeletal γ–Actin Perturbs Interaction of Actin Filaments with Myosin and ADF/Cofilin Family Proteins." Preprint. https://doi.org/10.7554/eLife.93013.1.

Greve, Johannes N., Frederic V. Schwäbe, Thomas Pokrant, Jan Faix, Nataliya Di Donato, Manuel H. Taft, and Dietmar J. Manstein. 2022. "Frameshift Mutation S368fs in the Gene Encoding Cytoskeletal β-Actin Leads to ACTB-Associated Syndromic Thrombocytopenia by Impairing Actin Dynamics." *European Journal of Cell Biology* 101 (2): 151216. https://doi.org/10.1016/j.ejcb.2022.151216.

Hall, D.H., Herndon, L.A., and Altun, Z. 2017. "Introduction to C. Elegans Embryo Anatomy." *WormAtlas*. https://doi.org/doi:10.3908/wormatlas.4.1.

Happle, Rudolf. 2017. "Becker's Nevus and Lethal Beta-Actin Mutations." *Journal of Investigative Dermatology* 137 (8): 1619–21. https://doi.org/10.1016/j.jid.2017.04.003.

Hayashi, Yuriko, Kanako Ono, and Shoichiro Ono. 2019. "Mutations in Caenorhabditis Elegans Actin, Which Are Equivalent to Human Cardiomyopathy Mutations, Cause Abnormal Actin Aggregation in Nematode Striated Muscle." *F1000Research* 8 (March):279. https://doi.org/10.12688/f1000research.18476.1.

Hoogewijs, David, Koen Houthoofd, Filip Matthijssens, Jo Vandesompele, and Jacques R Vanfleteren. 2008. "Selection and Validation of a Set of Reliable Reference Genes for Quantitative Sod Gene Expression Analysis in C. Elegans." *BMC Molecular Biology* 9 (1): 9. https://doi.org/10.1186/1471-2199-9-9.

Jumper, John, Richard Evans, Alexander Pritzel, Tim Green, Michael Figurnov, Olaf Ronneberger, Kathryn Tunyasuvunakool, et al. 2021. "Highly Accurate Protein Structure Prediction with AlphaFold." *Nature* 596 (7873): 583–89. https://doi.org/10.1038/s41586-021-03819-2.

Krause, Michael, Martha Wild, Brad Rosenzweig, and David Hirsh. 1989. "Wild-Type and Mutant Actin Genes in Caenorhabditis Elegans." *Journal of Molecular Biology* 208 (3): 381–92. https://doi.org/10.1016/0022-2836(89)90503-2.

Kruse, Karsten, Rémi Berthoz, Luca Barberi, Anne-Cécile Reymann, and Daniel Riveline. 2024. "Actomyosin Clusters as Active Units Shaping Living Matter." *Current Biology: CB* 34 (20): R1045–58. https://doi.org/10.1016/j.cub.2024.08.043.

Lai, Wing-Fu, and Wing-Tak Wong. 2020. "Roles of the Actin Cytoskeleton in Aging and Age-Associated Diseases." *Ageing Research Reviews* 58 (March):101021. https://doi.org/10.1016/j.arr.2020.101021.

Landel, C. P., M. Krause, R. H. Waterston, and D. Hirsh. 1984. "DNA Rearrangements of the Actin Gene Cluster in Caenorhabditis Elegans Accompany Reversion of Three Muscle Mutants." *Journal of Molecular Biology* 180 (3): 497–513. https://doi.org/10.1016/0022-2836(84)90024-x.

Lappalainen, Pekka, Tommi Kotila, Antoine Jégou, and Guillaume Romet-Lemonne. 2022. "Biochemical and Mechanical Regulation of Actin Dynamics." *Nature Reviews Molecular Cell Biology* 23 (12): 836–52. https://doi.org/10.1038/s41580-022-00508-4.

Latham, Sharissa L., Nadja Ehmke, Patrick Y. A. Reinke, Manuel H. Taft, Dorothee Eicke, Theresia Reindl, Werner Stenzel, et al. 2018. "Variants in Exons 5 and 6 of ACTB Cause Syndromic

Thrombocytopenia." *Nature Communications* 9 (1): 4250. https://doi.org/10.1038/s41467-018-06713-0.

Lesanpezeshki, Leila, Jennifer E. Hewitt, Ricardo Laranjeiro, Adam Antebi, Monica Driscoll, Nathaniel J. Szewczyk, Jerzy Blawzdziewicz, Carla M. R. Lacerda, and Siva A. Vanapalli. 2019. "Pluronic Gel-Based Burrowing Assay for Rapid Assessment of Neuromuscular Health in C. Elegans." *Scientific Reports* 9 (1): 15246. https://doi.org/10.1038/s41598-019-51608-9.

Ly, Kien, Suzanne J. Reid, and Russell G. Snell. 2015. "Rapid RNA Analysis of Individual Caenorhabditis Elegans." *MethodsX* 2:59–63. https://doi.org/10.1016/j.mex.2015.02.002.

MacQueen, A. J., J. J. Baggett, N. Perumov, R. A. Bauer, T. Januszewski, L. Schriefer, and J. A. Waddle. 2005. "ACT-5 Is an Essential Caenorhabditis Elegans Actin Required for Intestinal Microvilli Formation." *Molecular Biology of the Cell* 16 (7): 3247–59. https://doi.org/10.1091/mbc.e04-12-1061.

Markaki, Maria, and Nektarios Tavernarakis. 2010. "Modeling Human Diseases in *Caenorhabditis Elegans*." *Biotechnology Journal* 5 (12): 1261–76. https://doi.org/10.1002/biot.201000183.

Marston, Daniel J, and Bob Goldstein. 2006. "Actin-Based Forces Driving Embryonic Morphogenesis in Caenorhabditis Elegans." *Current Opinion in Genetics & Development* 16 (4): 392–98.

Michelot, Alphée, and David G Drubin. 2011. "Building Distinct Actin Filament Networks Review in a Common Cytoplasm." *Current Biology* 21 (14): R560–69.

Murrell, Michael, Patrick W Oakes, Martin Lenz, and Margaret L Gardel. 2015. "Forcing Cells into Shape: The Mechanics of Actomyosin Contractility." *Nature Publishing Group* 16 (8): 486–98.

Naganathan, Sundar Ram, Sebastian Fürthauer, Josana Rodriguez, Bruno Thomas Fievet, Frank Jülicher, Julie Ahringer, Carlo Vittorio Cannistraci, and Stephan W. Grill. 2018. "Morphogenetic Degeneracies in the Actomyosin Cortex." *eLife* 7 (October):e37677. https://doi.org/10.7554/eLife.37677.

Nance, Jeremy. 2005. "Gastrulation in C. Elegans." *WormBook*.

Ono, K. 2003. "Specific Requirement for Two ADF/Cofilin Isoforms in Distinct Actin-Dependent Processes in Caenorhabditis Elegans." *Journal of Cell Science* 116 (10): 2073–85.

Ono, Shoichiro. 2014. "Regulation of Structure and Function of Sarcomeric Actin Filaments in Striated Muscle of the Nematode *Caenorhabditis Elegans*." *The Anatomical Record* 297 (9): 1548–59. https://doi.org/10.1002/ar.22965.

Ono, Shoichiro, and David Pruyne. 2012. "Biochemical and Cell Biological Analysis of Actin in the Nematode Caenorhabditis Elegans." *METHODS* 56 (1): 11–17.

Oosterheert, Wout, Florian E. C. Blanc, Ankit Roy, Alexander Belyy, Micaela Boiero Sanders, Oliver Hofnagel, Gerhard Hummer, Peter Bieling, and Stefan Raunser. 2023. "Molecular Mechanisms of Inorganic-Phosphate Release from the Core and Barbed End of Actin Filaments." *Nature Structural & Molecular Biology* 30 (11): 1774–85. https://doi.org/10.1038/s41594-023-01101-9.

Pacquelet, Anne, Matthieu Jousseaume, Jocelyn Etienne, and Grégoire Michaux. 2019. "Simultaneous Regulation of Cytokinetic Furrow and Nucleus Positions by Cortical Tension Contributes to Proper DNA Segregation during Late Mitosis." *Current Biology* 29 (22): 3766-3777.e4. https://doi.org/10.1016/j.cub.2019.09.013.

Paix, A, A Folkmann, D Rasoloson, and G Seydoux. 2015. "High Efficiency, Homology-Directed Genome Editing in Caenorhabditis Elegans Using CRISPR-Cas9 Ribonucleoprotein Complexes." *Genetics* 201 (1): 47–54.

Parker, Francine, Thomas G. Baboolal, and Michelle Peckham. 2020. "Actin Mutations and Their Role in Disease." *International Journal of Molecular Sciences* 21 (9): 3371. https://doi.org/10.3390/ijms21093371.

Pasturel, Aurélien, Pierre-Olivier Strale, and Vincent Studer. 2020. "Tailoring Common Hydrogels into 3D Cell Culture Templates." *Advanced Healthcare Materials* 9 (18): 2000519. https://doi.org/10.1002/adhm.202000519.

Patrinostro, Xiaobai, Pallabi Roy, Angus Lindsay, Christopher M. Chamberlain, Lauren J. Sundby, Colby G. Starker, Daniel F. Voytas, James M. Ervasti, and Benjamin J. Perrin. 2018. "Essential Nucleotide- and Protein-Dependent Functions of *Actb* /β-Actin." *Proceedings of the National Academy of Sciences* 115 (31): 7973–78. https://doi.org/10.1073/pnas.1807895115.

Pettersen, Eric F., Thomas D. Goddard, Conrad C. Huang, Elaine C. Meng, Gregory S. Couch, Tristan I. Croll, John H. Morris, and Thomas E. Ferrin. 2021. "UCSF ChimeraX: Structure Visualization for Researchers, Educators, and Developers." *Protein Science: A Publication of the Protein Society* 30 (1): 70–82. https://doi.org/10.1002/pro.3943.

Polubothu, S., D. Abdin, M. Barysch, A. Thomas, N. Bulstrode, R. Evans, L. Solman, et al. 2020. "Dermatological Signs Lead to Discovery of Mosaic ACTB Variants in Segmental Odontomaxillary Dysplasia." *The British Journal of Dermatology* 183 (6): 1128–30. https://doi.org/10.1111/bjd.19339.

Priess, J. R., and D. I. Hirsh. 1986. "Caenorhabditis Elegans Morphogenesis: The Role of the Cytoskeleton in Elongation of the Embryo." *Developmental Biology* 117 (1): 156–73. https://doi.org/10.1016/0012-1606(86)90358-1.

Procaccio, Vincent, Gloria Salazar, Shoichiro Ono, Melanie L. Styers, Marla Gearing, Antonio Davila, Richard Jimenez, et al. 2006. "A Mutation of Beta -Actin That Alters Depolymerization Dynamics Is Associated with Autosomal Dominant Developmental Malformations, Deafness, and Dystonia." *American Journal of Human Genetics* 78 (6): 947–60. https://doi.org/10.1086/504271.

Quintin, Sophie, Shaohe Wang, Julien Pontabry, Ambre Bender, François Robin, Vincent Hyenne, Frédéric Landmann, Christelle Gally, Karen Oegema, and Michel Labouesse. 2018. "Correction: Non-Centrosomal Epidermal Microtubules Act in Parallel to LET-502/ROCK to Promote *C. Elegans* Elongation (Doi:10.1242/Dev.126615)." *Development* 145 (10): dev167262. https://doi.org/10.1242/dev.167262.

Reymann, Anne-Cecile, Fabio Staniscia, Anna Erzberger, Guillaume Salbreux, and Stephan W Grill. 2016. "Cortical Flow Aligns Actin Filaments to Form a Furrow." *eLife* 5 (October):e17807.

Reynolds, Matthew J., Carla Hachicho, Ayala G. Carl, Rui Gong, and Gregory M. Alushin. 2022. "Bending Forces and Nucleotide State Jointly Regulate F-Actin Structure." *Nature* 611 (7935): 380–86. https://doi.org/10.1038/s41586-022-05366-w.

Riva, Claudia, Martina Hajduskova, Christelle Gally, Shashi Kumar Suman, Arnaud Ahier, and Sophie Jarriault. 2022. "A Natural Transdifferentiation Event Involving Mitosis Is Empowered by Integrating Signaling Inputs with Conserved Plasticity Factors." *Cell Reports* 40 (12): 111365. https://doi.org/10.1016/j.celrep.2022.111365.

Rivière, Jean-Baptiste, Bregje W M Van Bon, Alexander Hoischen, Stanislav S Kholmanskikh, Brian J O'Roak, Christian Gilissen, Sabine Gijsen, et al. 2012. "De Novo Mutations in the Actin Genes ACTB and ACTG1 Cause Baraitser-Winter Syndrome." *Nature Genetics* 44 (4): 440–44. https://doi.org/10.1038/ng.1091.

Rodriguez, Alexis, and Anna Kashina. 2018. "Posttranscriptional and Posttranslational Regulation of Actin." *Anatomical Record (Hoboken, N.J. : 2007)* 301 (12): 1991–98. https://doi.org/10.1002/ar.23958.

Rose, Lesilee, and Pierre Gönczy. 2014. "Polarity Establishment, Asymmetric Division and Segregation of Fate Determinants in Early C. Elegans Embryos." *WormBook*, 1–43.

Rubenstein, Peter A., and Kuo-Kuang Wen. 2014. "Insights into the Effects of Disease-causing Mutations in Human Actins." *Cytoskeleton* 71 (4): 211–29. https://doi.org/10.1002/cm.21169.

Schafer, William. 2005. “Egg-Laying.” *WormBook*.
Schutt, Clarence E., James C. Myslik, Michael D. Rozycki, Nalin C. W. Goonesekere, and Uno Lindberg. 1993. “The Structure of Crystalline Profilin–β-Actin.” *Nature* 365 (6449): 810–16. https://doi.org/10.1038/365810a0.
Serobyan, Vahan, Zacharias Kontarakis, Mohamed A El-Brolosy, Jordan M Welker, Oleg Tolstenkov, Amr M Saadeldein, Nicholas Retzer, Alexander Gottschalk, Ann M Wehman, and Didier Yr Stainier. 2020. “Transcriptional Adaptation in Caenorhabditis Elegans.” *eLife* 9 (January):e50014. https://doi.org/10.7554/eLife.50014.
Skogseid, Inger Marie, Oddveig Røsby, Ane Konglund, James P. Connelly, Bård Nedregaard, Greg Eigner Jablonski, Nadja Kvernmo, Asbjørg Stray-Pedersen, and Joel C. Glover. 2018. “Dystonia-Deafness Syndrome Caused by ACTB p.Arg183Trp Heterozygosity Shows Striatal Dopaminergic Dysfunction and Response to Pallidal Stimulation.” *Journal of Neurodevelopmental Disorders* 10 (1): 17. https://doi.org/10.1186/s11689-018-9235-z.
Skruber, Kristen, Tracy-Ann Read, and Eric A Vitriol. 2018. “Reconsidering an Active Role for G-Actin in Cytoskeletal Regulation.” *Journal of Cell Science* 131 (1): jcs203760-11.
Tondeleir, Davina, Anja Lambrechts, Matthias Müller, Veronique Jonckheere, Thierry Doll, Drieke Vandamme, Karima Bakkali, et al. 2012. “Cells Lacking β-Actin Are Genetically Reprogrammed and Maintain Conditional Migratory Capacity*.” *Molecular & Cellular Proteomics* 11 (8): 255–71. https://doi.org/10.1074/mcp.M111.015099.
Vanslembrouck, Bieke, Christophe Ampe, and Jolanda Van Hengel. 2020. “Time for Rethinking the Different B-actin Transgenic Mouse Models?” *Cytoskeleton* 77 (12): 527–43. https://doi.org/10.1002/cm.21647.
Vedula, Pavan, Satoshi Kurosaka, Nicolae Adrian Leu, Yuri I Wolf, Svetlana A Shabalina, Junling Wang, Stephanie Sterling, Dawei W Dong, and Anna Kashina. 2017. “Diverse Functions of Homologous Actin Isoforms Are Defined by Their Nucleotide, Rather than Their Amino Acid Sequence.” *eLife* 6 (December):e31661. https://doi.org/10.7554/eLife.31661.
Verloes, Alain, Nataliya Di Donato, Julien Masliah-Planchon, Marjolijn Jongmans, Omar A. Abdul-Raman, Beate Albrecht, Judith Allanson, et al. 2015. “Baraitser–Winter Cerebrofrontofacial Syndrome: Delineation of the Spectrum in 42 Cases.” *European Journal of Human Genetics* 23 (3): 292–301. https://doi.org/10.1038/ejhg.2014.95.
Verloes, Alain, Séverine Drunat, Daniela Pilz, and Nataliya Di Donato. 1993. “Baraitser-Winter Cerebrofrontofacial Syndrome.” In *GeneReviews®*, edited by Margaret P. Adam, Jerry Feldman, Ghayda M. Mirzaa, Roberta A. Pagon, Stephanie E. Wallace, Lora JH Bean, Karen W. Gripp, and Anne Amemiya. Seattle (WA): University of Washington, Seattle. http://www.ncbi.nlm.nih.gov/books/NBK327153/.
Vontell, Regina, Veena G. Supramaniam, Alice Davidson, Claire Thornton, Andreas Marnerides, Muriel Holder-Espinasse, Suzanne Lillis, et al. 2019. “Post-Mortem Characterisation of a Case With an ACTG1 Variant, Agenesis of the Corpus Callosum and Neuronal Heterotopia.” *Frontiers in Physiology* 10. https://www.frontiersin.org/journals/physiology/articles/10.3389/fphys.2019.00623.
Vuong-Brender, Thanh Thi Kim, Martine Ben Amar, Julien Pontabry, and Michel Labouesse. 2017. “The Interplay of Stiffness and Force Anisotropies Drives Embryo Elongation.” *eLife* 6 (February):e23866. https://doi.org/10.7554/eLife.23866.
Vuong-Brender, Thanh T.K., Xinyi Yang, and Michel Labouesse. 2016. “C. Elegans Embryonic Morphogenesis.” In *Current Topics in Developmental Biology*, 116:597–616. Elsevier. https://doi.org/10.1016/bs.ctdb.2015.11.012.

Waliman, Matthew, Ryan L. Johnson, Gunalan Natesan, Neil A. Peinado, Shiqin Tan, Anthony Santella, Ray L. Hong, and Pavak K. Shah. 2024. "Automated Cell Lineage Reconstruction Using Label-Free 4D Microscopy." *Genetics* 228 (2): iyae135. https://doi.org/10.1093/genetics/iyae135.

Wang, Shaohe, Stacy D. Ochoa, Renat N. Khaliullin, Adina Gerson-Gurwitz, Jeffrey M. Hendel, Zhiling Zhao, Ronald Biggs, et al. 2019. "A High-Content Imaging Approach to Profile *C. Elegans* Embryonic Development." *Development* 146 (7): dev174029. https://doi.org/10.1242/dev.174029.

Waterhouse, Andrew, Martino Bertoni, Stefan Bienert, Gabriel Studer, Gerardo Tauriello, Rafal Gumienny, Florian T Heer, et al. 2018. "SWISS-MODEL: Homology Modelling of Protein Structures and Complexes." *Nucleic Acids Research* 46 (W1): W296–303. https://doi.org/10.1093/nar/gky427.

Welker, Jordan M., Vahan Serobyan, Elhamalsadat Zaker Esfahani, and Didier Y. R. Stainier. 2023. "Partial Sequence Identity in a 25-Nucleotide Long Element Is Sufficient for Transcriptional Adaptation in the Caenorhabditis Elegans Act-5/Act-3 Model." *PLoS Genetics* 19 (6): e1010806. https://doi.org/10.1371/journal.pgen.1010806.

Wilkinson, Alex W., Jonathan Diep, Shaobo Dai, Shuo Liu, Yaw Shin Ooi, Dan Song, Tie-Mei Li, et al. 2019. "SETD3 Is an Actin Histidine Methyltransferase That Prevents Primary Dystocia." *Nature* 565 (7739): 372–76. https://doi.org/10.1038/s41586-018-0821-8.

Willis, John H., Edwin Munro, Rebecca Lyczak, and Bruce Bowerman. 2006. "Conditional Dominant Mutations in the Caenorhabditis Elegans Gene Act-2 Identify Cytoplasmic and Muscle Roles for a Redundant Actin Isoform." *Molecular Biology of the Cell* 17 (3): 1051–64. https://doi.org/10.1091/mbc.e05-09-0886.

Xiao, Long, Duchangjiang Fan, Huan Qi, Yulin Cong, and Zhuo Du. 2022. "Defect-Buffering Cellular Plasticity Increases Robustness of Metazoan Embryogenesis." *Cell Systems* 13 (8): 615-630.e9. https://doi.org/10.1016/j.cels.2022.07.001.

Yemini, Eviatar, Tadas Jucikas, Laura J. Grundy, André E.X. Brown, and William R. Schafer. 2013. "A Database of C. Elegans Behavioral Phenotypes." *Nature Methods* 10 (9): 877–79. https://doi.org/10.1038/nmeth.2560.

Yemini, Eviatar, Albert Lin, Amin Nejatbakhsh, Erdem Varol, Ruoxi Sun, Gonzalo E. Mena, Aravinthan D.T. Samuel, Liam Paninski, Vivek Venkatachalam, and Oliver Hobert. 2021. "NeuroPAL: A Multicolor Atlas for Whole-Brain Neuronal Identification in C. Elegans." *Cell* 184 (1): 272-288.e11. https://doi.org/10.1016/j.cell.2020.12.012.

Zech, Michael, Robert Jech, Matias Wagner, Tobias Mantel, Sylvia Boesch, Michael Nocker, Angela Jochim, et al. 2017. "Molecular Diversity of Combined and Complex Dystonia: Insights from Diagnostic Exome Sequencing." *Neurogenetics* 18 (4): 195–205. https://doi.org/10.1007/s10048-017-0521-9.

Zhang, Pu, Taylor N. Medwig-Kinney, and Bob Goldstein. 2023. "Architecture of the Cortical Actomyosin Network Driving Apical Constriction in *C. Elegans*." *Journal of Cell Biology* 222 (9): e202302102. https://doi.org/10.1083/jcb.202302102.

Figure legends

Figure 1 : Insertion of Non-Muscle Actinopathies variants in the *C. elegans act-2*

(A) Dot heatmap of patients' symptoms. Intellectual disability (ID) level letter code : n=none, m=mild, mo=moderate, s=severe, p=profound. MRI = Magnetic Resonance Imaging. BWCFF = Baraitser-Winter Cerebro Fronto Facial syndrome. (B) Structural model of ACT-2 G-actin generated by Alphafold2. Subdomains of ACT-2 are coloured in grey (SD1), light grey (SD2), blue (SD3) and light blue (SD4). (Right) Homology model of the ACT-2 filament (based on PDB-ID: 8DNH). ACT-2 protomers are coloured in different shades of blue. The mutated residues investigated in this study are shown in red. The ATP bound to the individual protomers is shown as a stick-model. The zoom-in shows the location and structural environment of the individual mutated residues in more detail. (C) Schematic *act-2* representation highlighting the loci of single point variants obtained via CRISPR edition. Three *act-2* gene knockout alleles are also depicted: *rey016*, *rey021* and *ok1229* (Willis et al., 2006). Note that the amino acid numbering is here in frame with human ACTB/ACTG1, consider -1 AA in the frame of *C. elegans* due to an additional cysteine in second N-ter position, the base pair are however kept in the *C. elegans act-2* frame. (D) Table summarizing the overall viability of *C. elegans act-2* variants at 20°C.

Figure S1 :

(A) Amino acid alignment of *C. elegans'* ACT-2, human ACTB and ACTG1 showing high conservation of amino acid as well as amino acid physico-chemical properties (Snapgene). Loci of interest are framed with black boxes. (B) Alignment of sequences obtained from the sequencing of F1 animals from the CRISPR/Cas9 *act-2* p.G74V generation show the presence of the Gly to Ser variant (Snapgene, black box). Top rows show the reference *act-2* sequence and its translation. Bottom rows show the obtained sequence, peaks and predicted translation.

Figure 2 : *act-2* gene knock-outs affects fertility despite compensation mechanisms

(A) Single animal RT-qPCR showing the normalized amount of mRNA for each *C. elegans* actin coding genes in *act-2*(*ok1229)* and *act-2*(*rey021)* homozygotes. Normalization was done with the amount of mRNA quantified for the housekeeping gene *iscu-1* and with the WT values set to 1. Different colours show different replicates. Small dot is the value for one animal while bigger dots correspond to the experiment's mean. Diamonds show the mean of all replicates. (B) Progeny number of homozygous *act-2* knockout (*ok1229* and *rey021*) animals at the mentioned temperatures were counted during 48h. The sum of eggs laid for one animal is shown as a dot or a triangle, overlaid by standardised boxplots and mean values represented by a diamond. (B') Percentage of eggs that failed to hatch. The mean number of eggs that did not hatch for one animal is shown as a dot or a triangle, overlaid by standardised boxplots and mean values represented by a diamond. The rightmost plot presents the 95% credibility intervals of the posterior distributions of the embryonic lethality rates considering low informative priors described in the methods section and our observed data set. These are calculated with a Bayesian model based on Poisson laws with an offset to account for the progeny numbers. Experimental values are represented by red diamonds (mean) and blue circles (median). (C) Progeny number at 20°C were counted for 72h for homozygous (*rey016*/*rey016*) (*rey021*/*rey021*) or heterozygous (*rey016*/+) (*rey021*/+) *act-2* KO animals. The sum of eggs laid for one animal is shown as a dot, overlaied by standardised boxplots and mean values represented by a diamond. (C') Percentage of eggs that failed to hatch. The mean number of eggs that did not hatch for one animal is shown

as a dot, overlaid by standardised boxplots and mean values represented by a diamond. The rightmost plot presents the 95% credibility intervals of the posterior distributions of the embryonic lethality rates considering low informative priors described in the methods section and our observed data set. These are calculated with a Bayesian model based on Poisson laws with an offset to account for the progeny numbers. Experimental values are represented by red diamonds (mean) and blue circles (median). (B,B',C,C') Boxplots display the maximum and minimum values, the median as well as first and third quartiles.

Figure S2 :

(A) Standard curve analysis to determine the efficiency of amplification of the 6 primer pairs used for RT-qPCR. Efficiency is calculated using $E = 10^{\frac{1}{slope}}$.

Figure 3 : *act-2* variants affect egg-laying capacities and embryogenesis success

(A) Progeny number at 20°C were counted for 72h for homozygous *act-2* variants. The sum of eggs laid for one animal is shown as a dot, overlaid by standardised boxplots and mean values represented by a diamond. (B) Percentage of eggs that failed to hatch. The percent of dead eggs for one animal is shown as a dot, overlaid by standardised boxplots and mean values represented by a diamond. Boxplots display the maximum and minimum values, the median as well as first and third quartiles. The rightmost plot presents the 95% credibility intervals of the posterior distributions of the embryonic lethality rates considering the priors described in the methods section and our observed data set. These are calculated with a Bayesian model based on Poisson laws with an offset to account for the progeny numbers. Experimental values are represented by red diamonds (mean) and blue circles (median). (C) Actin organization in a WT gonad observed using an actin probe (LifeAct::mKate2), max projection of a Z-series of images. Green and purple arrows illustrate the space measured to calculate the rachis/gonad ratio measured in front of the -1 oocyte. Scale bar is 20µm. (D) Boxplot presenting the ratio between the rachis and the gonad's width of homozygote animals. Mean is represented as a diamond. (E) Heatmap of observed phenotypes, in percent. (F) Stacked histogram of the end status of embryogenesis for different *act-2* variants in percent. Schemes on the left represent the different defects observed. * embryos coming from heterozygous balanced animals. (See Movies 1, 2, 3, 4 and 5).

Figure S3 :

(A) Progeny number at 20°C were counted for 72h for heterozygous *act-2* variant animals. The sum of eggs laid for one animal is shown as a dot, overlaid by standardised boxplots and mean values represented by a diamond. (B) Percentage of eggs that failed to hatch. The percent of dead eggs for one animal is shown as a dot, overlaid by standardised boxplots and mean values are represented by a diamond. (C, D) Red boxes show the area where no WT eggshells are present. Red points show embryos that did not complete embryogenesis while blue triangles represent a successful embryogenesis. Embryo schemes above are at the right scale. * embryos coming from heterozygous balanced animals. (C) Aspect ratio measurement of embryos' eggshell. Aspect ratio is defined as the ratio between the major and minor axis. (D) 2D Area measurement of embryos' eggshell. E. Timeline of recognizable morphogenesis stages during *C. elegans'* embryogenesis. Time counted after fertilization, from (Hall, D.H., Herndon, L.A., and Altun, Z. 2017). Leftmost plot presents the timing in minutes between the bean stage and the

comma stage. Rightmost plot presents the timing in minutes between the comma stage and hatching. * embryos coming from heterozygous balanced animals.

Figure 4 : Actin mutation effects on cortical organization in early embryos

(A) Cortical plane of embryos at different stages, LifeAct::mKate2 shown in magenta and NMY-2::GFP shown in green, to reveal actin filaments and myosin distribution. p.T203M animals only have LifeAct::mKate2. (PN = Pronuclei) Anterior is on the left. (B, C, D) Equatorial plane image of embryos expressing LifeAct::mKate2 (magenta) and NMY-2::GFP (green). (B) Cytokinesis defect observed. The cytokinesis ring relaxes after completion of a first ingression (pink arrow), this is followed by multiple simultaneous ingressions as the cell proceeds to divide directly into four daughter cells. See Movie 6. (C) Meiosis defects. An additional nucleus is visible (blue arrow). Nuclei are circled. See Movie 7. (D) Blebbing. Large protrusion called bleb extrude from the anterior cell (orange arrow). After actin and myosin reassembly, the bleb retracted and division seemed to occur normally. See Movie 8. (E) Abnormal membrane ruffling is observed in some embryos (white arrow). (F) Cortical plane of embryos presenting other phenotypes. Abnormal aspect ratio of the cortex implies a rounder embryo (see also Figure S4). Abnormal division axis (red arrows) leads to abnormal cell-cell contacts. Breaks in cortex are highlighted by green arrows. Scale bar is 10µm.

Figure S4 :

Size of the anterior cell AB (Magenta arrow) divided by the embryo's size (Green arrow) in percent. Boxplots display: the maximum and minimum values, the median as well as first and third quartiles.

Figure 5 : Actin mutations can affect motility and/or neuronal cell number

(A) 3D animal migration assay. Percentage of animals reaching a chemoattractant after migration inside a pluronic gel, monitored every 15 minutes for 2 hours. Results for individual wells (N) for each variant are visible as transparent dots, n is the total number of animals assessed and bars show the standard deviation. The final proportion for each variant was compared to that of WT in the frame of Bayesian statistics, using two binomial distributions. The odds ratio (OR) as well as the probability (p) that the difference is superior to 0.2 are indicated. (B) Variation of the neuronal cell number are observed in *act-2* variant conditions. Reconstructed image of an animal expressing the NeuroPal transgene. Insets show representative images of identified defects compared to the WT *act-2* reference: presence of a micronucleus (Orange), an extra (Magenta) or a missing cell (Green). Scale bar is 50 µm. (C) Summary of neuronal phenotypes observed in the actin variants.

Figure S5 :

Chemotaxis assay. The chemotaxis index is calculated $I = \frac{n_{OP50} - n_{H_2O}}{n_{Total} - n_{immobile\ animals}}$ and show the proportion of animals chemoattracted to concentrated OP50 (100mg/mL) (in red). Blue bars show the percentage of animals that did not move from where they were placed for the assay.

Figure 6 : Data integration to build a comparative tool

(A) Principal Component Analysis plot of analysed actin variant animals reveal clusters which can be associated to classes of phenotypes. Corresponding table with data is available in Figure S6A. p.G74V was added manually as no data could be retrieved for this strain. Arrows link

homozygotes to their respective heterozygotes. (B) Distances calculated between each actin variant and the WT reference in the two first dimensions.

Figure S6 :

(A) Variables factor map used to build the Principal Component Analysis plot in the two first dimensions. The Variables factor map presents a view of the projection of the observed variables projected into the plane spanned by the first two principal components. (B) Matrix of variables presented in Figure 6A, as well as their quality of representation in each dimension (cos2). (B) Principal Component Analysis plot of analysed actin variant animals using only the variables quantified without introducing fluorescent reporters in the actin variant background. Arrows link homozygotes to their respective heterozygotes. (D) Variables presented in S6C, as well as their quality of representation in each dimension (cos2). (E) Principal Component Analysis plot of analysed actin variant animals without p.T203M and p.R147S variations. (F) Variables presented in S6E, as well as their quality of representation in each dimension (cos2).

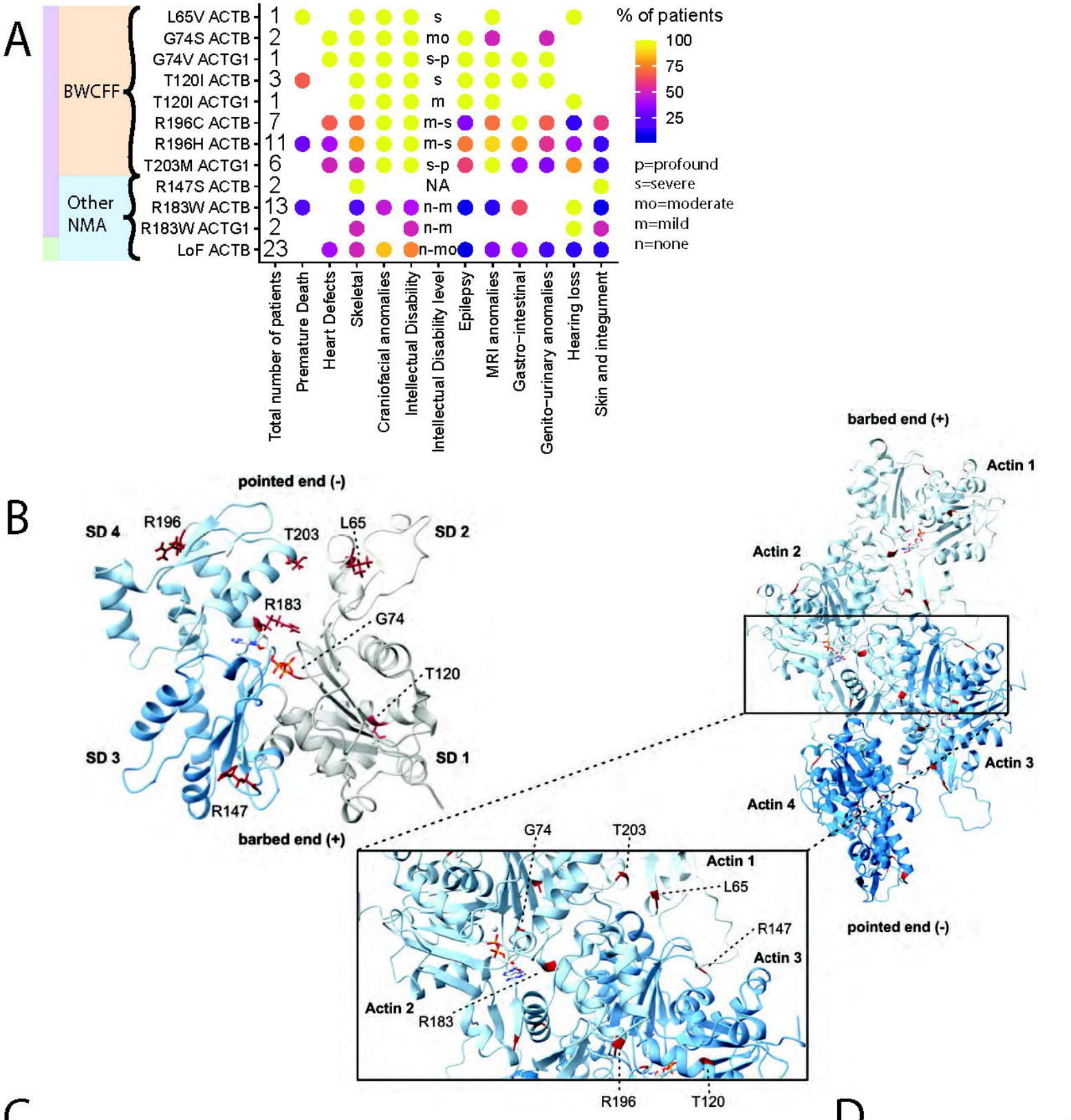

act-2 variant	*C. elegans* variant viability
p.L65V	Homozygote
p.G74S	Homozygote
p.G74V	Not viable
p.T120I	Homozygote
p.R196C	Homozygote
p.R196H	Homozygote
p.T203M	Heterozygote
KO *ok1229*	Homozygote
KO *rey016*	Homozygote
KO *rey021*	Homozygote
p.R147S	Heterozygote
p.R183W	Homozygote

Figure 1

A

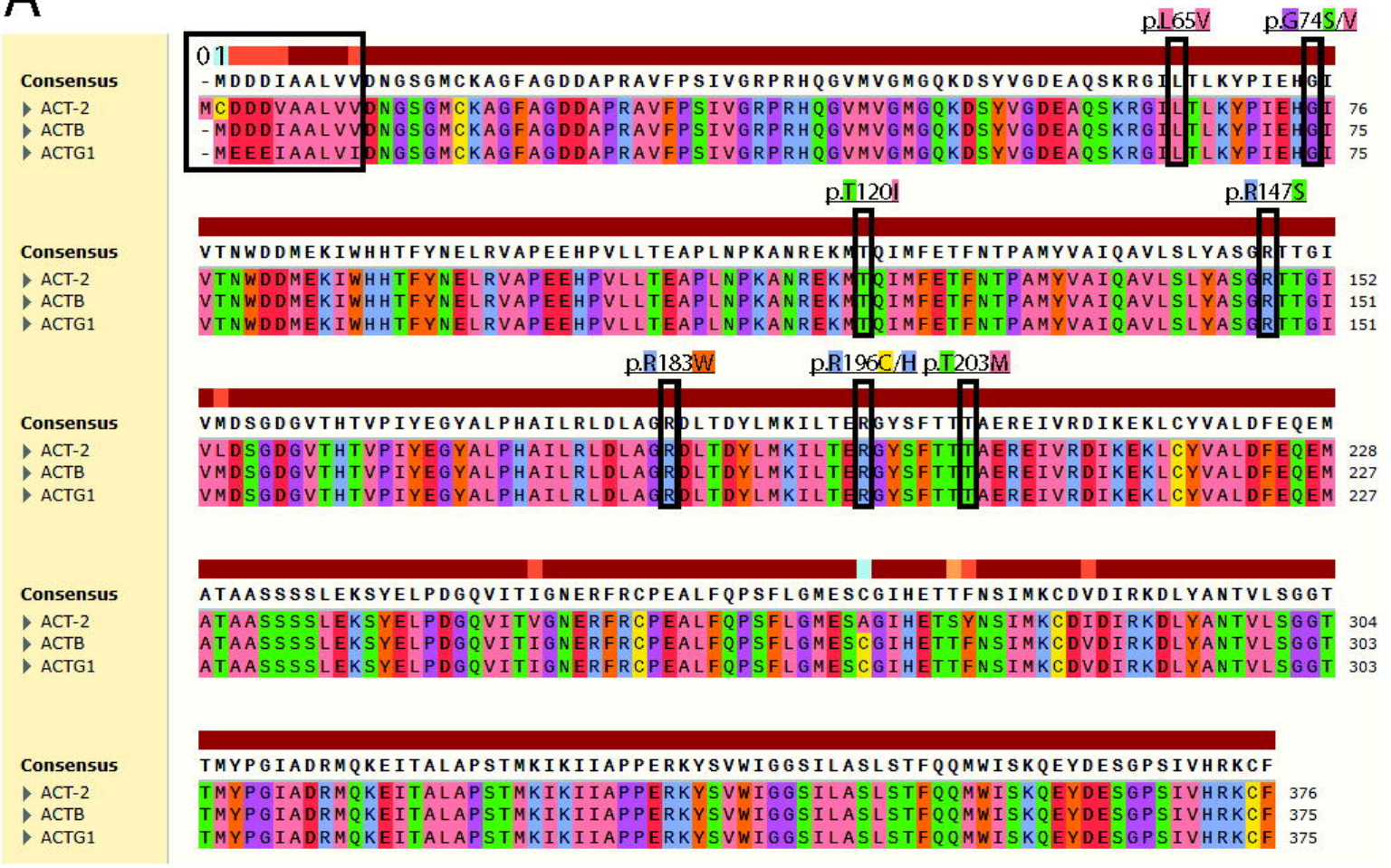
p.L65V
p.G74S/V
Consensus
ACT-2
ACTB
ACTG1
p.T120I
p.R147S
p.R183W
p.R196C/H
p.T203M

B

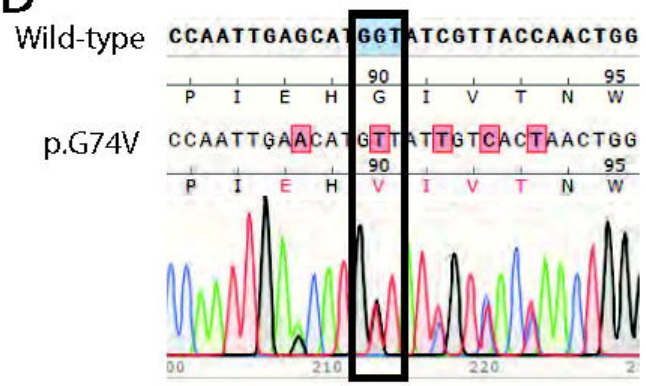
Wild-type
CCAATTGAGCATGGTATCGTTACCAACTGG
p.G74V
CCAATTGAACATGTTATTGTCACTAACTGG

Figure S1

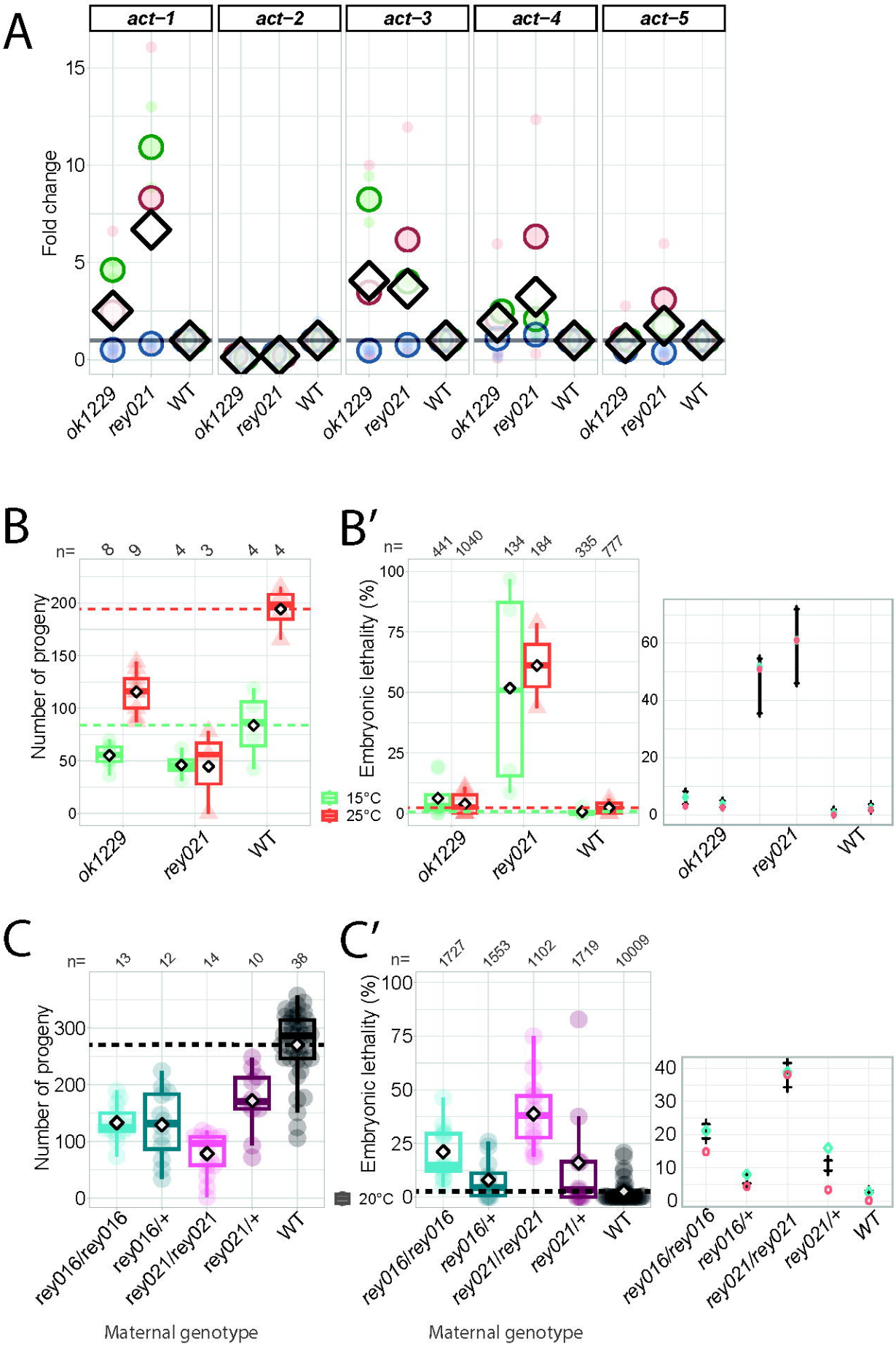
A
act−1
act−2
act−3
act−4
act−5
Fold change
ok1229
rey021
WT
B
n=
8 9 4 3 4 4
Number of progeny
B′
n=
441 1040 134 184 335 777
Embryonic lethality (%)
15°C
25°C
C
n=
13 12 14 10 38
Number of progeny
rey016/rey016
rey016/+
rey021/rey021
rey021/+
Maternal genotype
C′
n=
1727 1553 1102 1719 10009
Embryonic lethality (%)
20°C

Figure 2

$$E = 10^{\frac{1}{slope}}$$

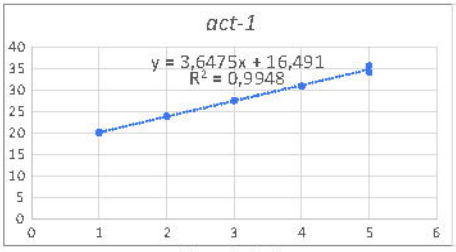

E = 1.88

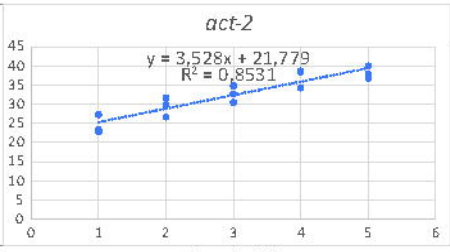

E = 1.92

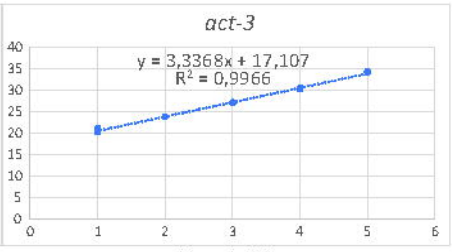

E = 1.99

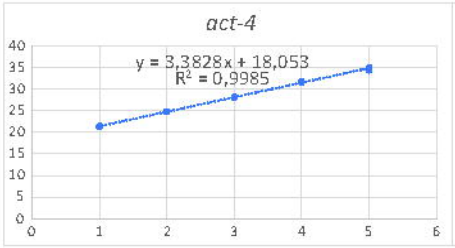

E = 1.97

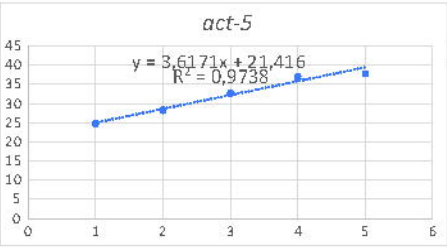

E = 1.89

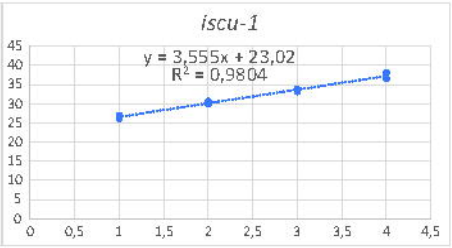

E = 1.91

Figure S2

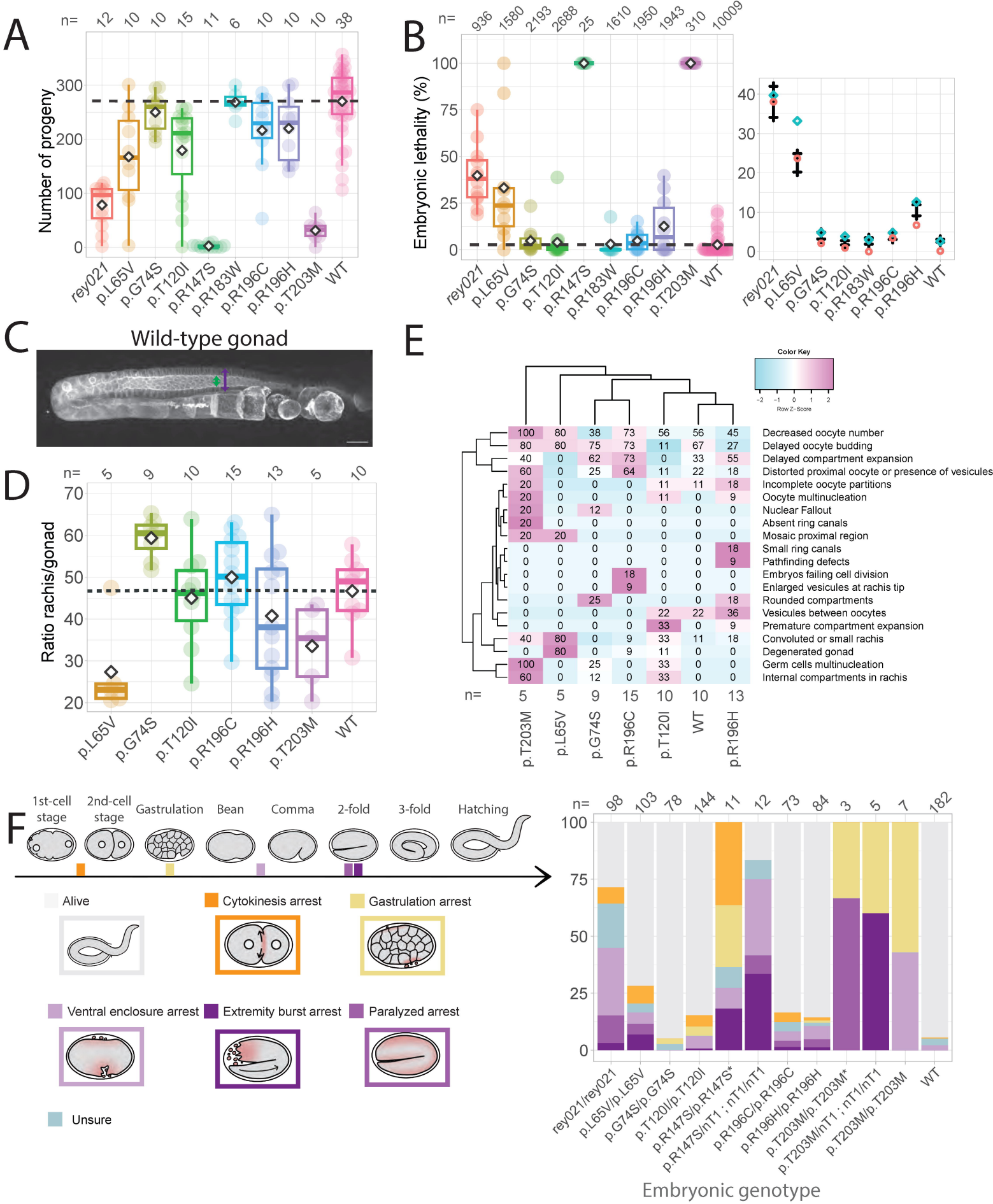
A
n= 12 10 10 15 11 6 10 10 10 38
Number of progeny
0 100 200 300
rey021 p.L65V p.G74S p.T120I p.R147S p.R183W p.R196C p.R196H p.T203M WT
B
n= 936 1580 2193 2688 25 1610 1950 1943 310 10009
Embryonic lethality (%)
0 25 50 75 100
0 10 20 30 40
rey021 p.L65V p.G74S p.T120I p.R147S p.R183W p.R196C p.R196H p.T203M WT
C
Wild-type gonad
D
n= 5 9 10 15 13 5 10
Ratio rachis/gonad
20 30 40 50 60 70
p.L65V p.G74S p.T120I p.R196C p.R196H p.T203M WT
E
Color Key
Row Z-Score
Decreased oocyte number 100 80 38 73 56 56 45
Delayed oocyte budding 80 80 75 73 11 67 27
Delayed compartment expansion 40 0 62 73 0 33 55
Distorted proximal oocyte or presence of vesicules 60 0 25 64 11 22 18
Incomplete oocyte partitions 20 0 0 0 11 11 18
Oocyte multinucleation 20 0 0 0 11 0 9
Nuclear Fallout 20 0 12 0 0 0 0
Absent ring canals 20 0 0 0 0 0 0
Mosaic proximal region 20 20 0 0 0 0 0
Small ring canals 0 0 0 0 0 0 18
Pathfinding defects 0 0 0 0 0 0 9
Embryos failing cell division 0 0 0 18 0 0 0
Enlarged vesicules at rachis tip 0 0 0 9 0 0 0
Rounded compartments 0 0 25 0 0 0 18
Vesicules between oocytes 0 0 0 0 22 22 36
Premature compartment expansion 0 0 0 0 33 0 9
Convoluted or small rachis 40 80 0 9 33 11 18
Degenerated gonad 0 80 0 9 11 0 0
Germ cells multinucleation 100 0 25 0 33 0 0
Internal compartments in rachis 60 0 12 0 33 0 0
n= 5 5 9 15 10 10 13
p.T203M p.L65V p.G74S p.R196C p.T120I WT p.R196H
F
1st-cell stage
2nd-cell stage
Gastrulation
Bean
Comma
2-fold
3-fold
Hatching
Alive
Cytokinesis arrest
Gastrulation arrest
Ventral enclosure arrest
Extremity burst arrest
Paralyzed arrest
Unsure
n= 98 103 78 144 11 12 73 84 3 5 7 182
0 25 50 75 100
rey021/rey021
p.L65V/p.L65V
p.G74S/p.G74S
p.T120I/p.T120I
p.R147S/p.R147S*
p.R147S/nT1 ; nT1/nT1
p.R196C/p.R196C
p.R196H/p.R196H
p.T203M/p.T203M*
p.T203M/nT1 ; nT1/nT1
p.T203M/p.T203M
WT
Embryonic genotype

Figure 3

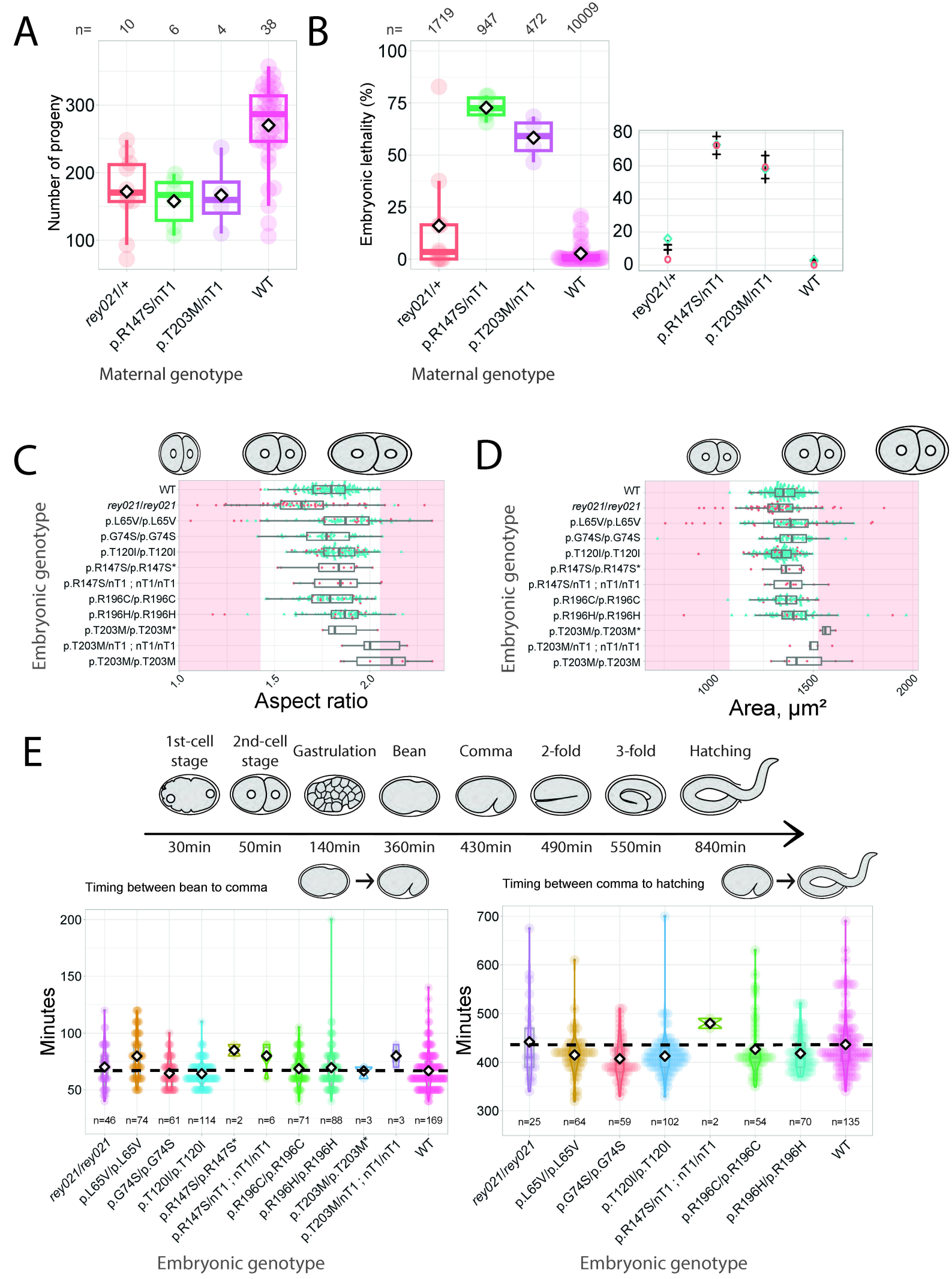
A
n= 10 6 4 38
Number of progeny
100
200
300
rey021/+
p.R147S/nT1
p.T203M/nT1
WT
Maternal genotype
B
n= 1719 947 472 10009
Embryonic lethality (%)
0
25
50
75
100
80
60
40
20
0
rey021/+
p.R147S/nT1
p.T203M/nT1
WT
Maternal genotype
C
Embryonic genotype
WT
rey021/rey021
p.L65V/p.L65V
p.G74S/p.G74S
p.T120I/p.T120I
p.R147S/p.R147S*
p.R147S/nT1 ; nT1/nT1
p.R196C/p.R196C
p.R196H/p.R196H
p.T203M/p.T203M*
p.T203M/nT1 ; nT1/nT1
p.T203M/p.T203M
1.0
1.5
2.0
Aspect ratio
D
Embryonic genotype
1000
1500
2000
Area, µm²
E
1st-cell stage
2nd-cell stage
Gastrulation
Bean
Comma
2-fold
3-fold
Hatching
30min
50min
140min
360min
430min
490min
550min
840min
Timing between bean to comma
Timing between comma to hatching
Minutes
50
100
150
200
n=46 n=74 n=61 n=114 n=2 n=6 n=71 n=88 n=3 n=3 n=169
Minutes
300
400
500
600
700
n=25 n=64 n=59 n=102 n=2 n=54 n=70 n=135
Embryonic genotype
Embryonic genotype

Figure S3

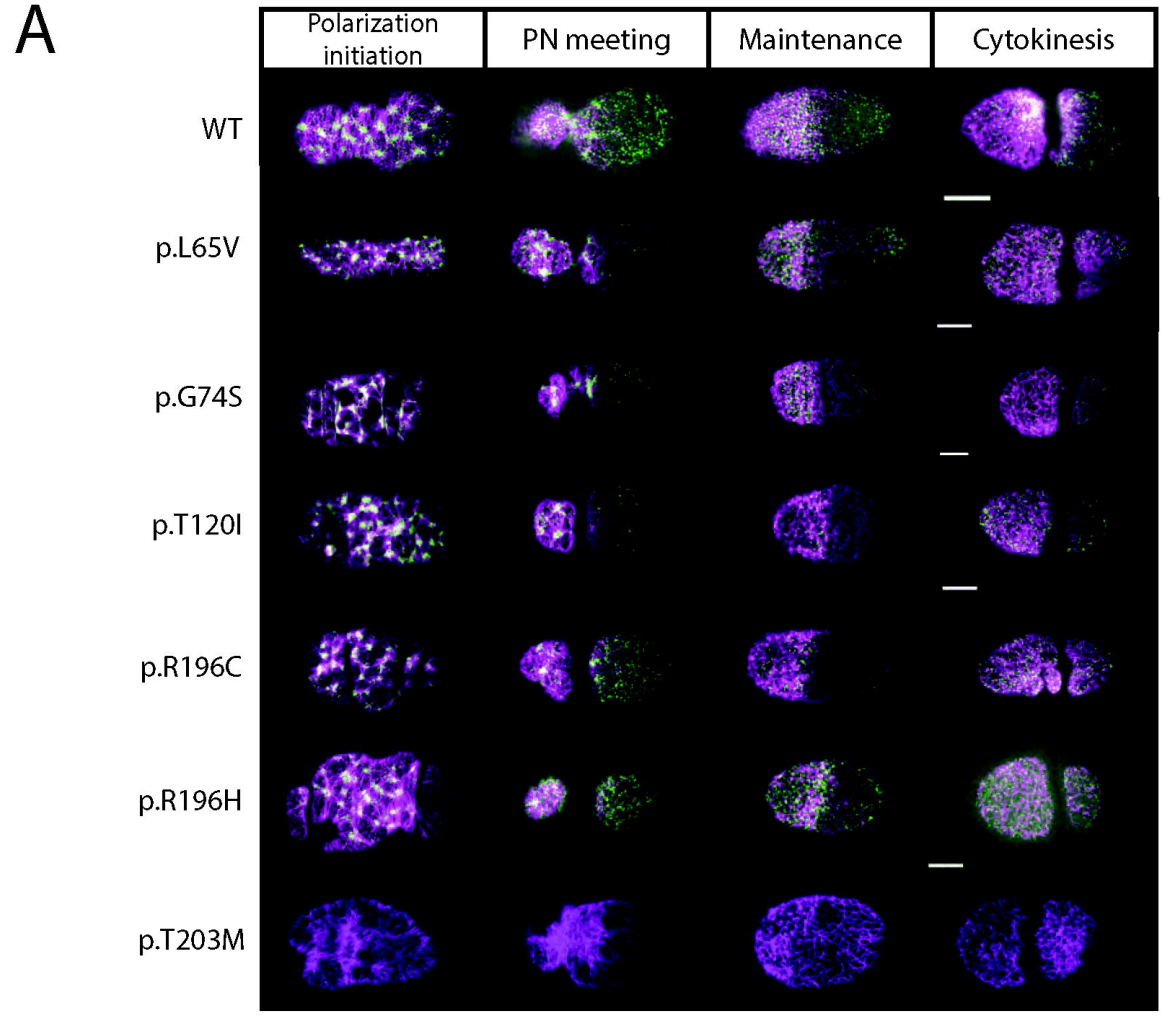

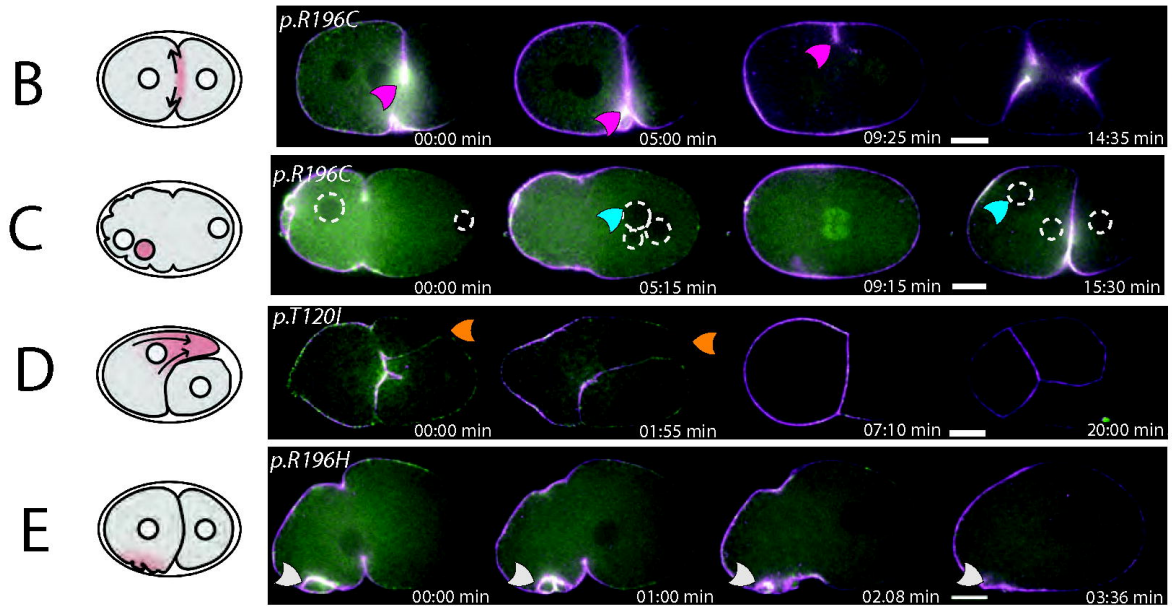

L65V	G74S	T120I	R196C	R196H	T203M*	WT
1/7	1/5	0/4	2/12	0/9	3/6	0/10

L65V	G74S	T120I	R196C	R196H	T203M*	WT
6/7	2/5	1/4	7/12	2/9	0/6	1/10

L65V	G74S	T120I	R196C	R196H	T203M*	WT
3/7	0/5	2/4	1/12	1/9	2/6	0/10

L65V	G74S	T120I	R196C	R196H	T203M*	WT
0/7	0/5	3/4	0/12	1/9	0/6	0/10

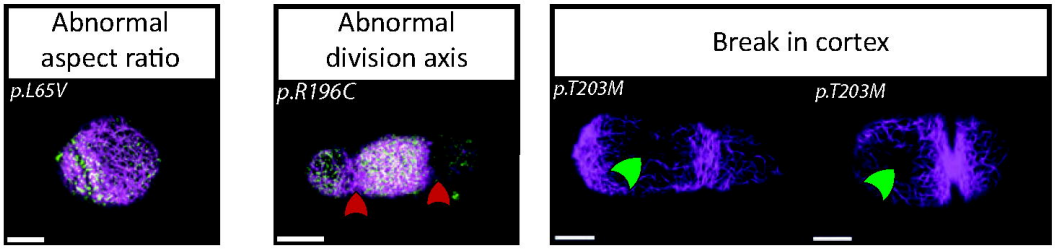

Figure 4

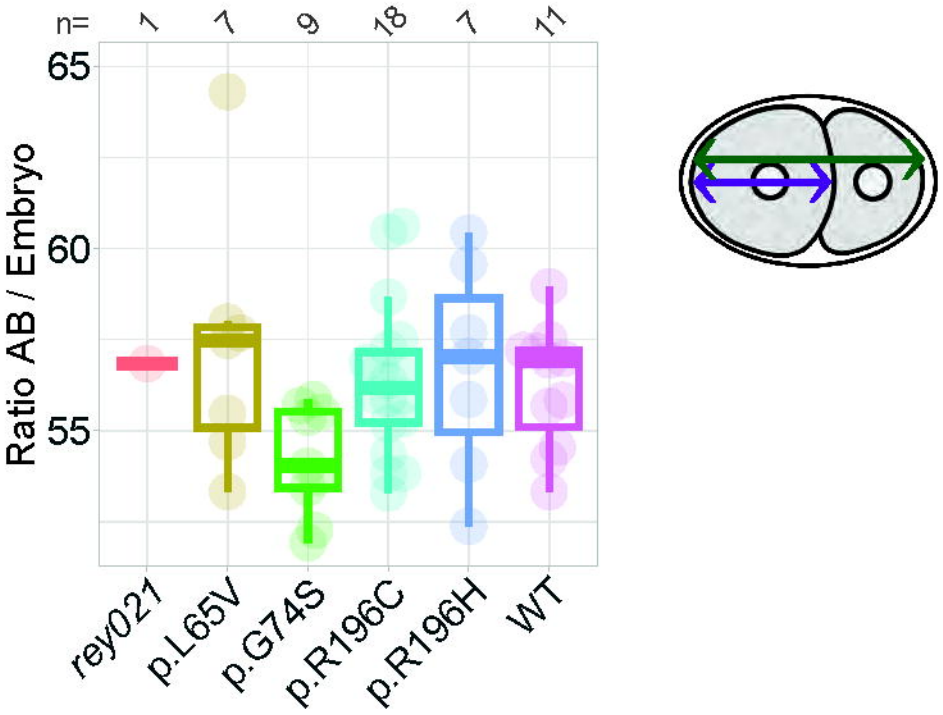
n=
1
7
9
18
7
11
65
60
55
Ratio AB / Embryo
rey021
p.L65V
p.G74S
p.R196C
p.R196H
WT

Figure S4

A

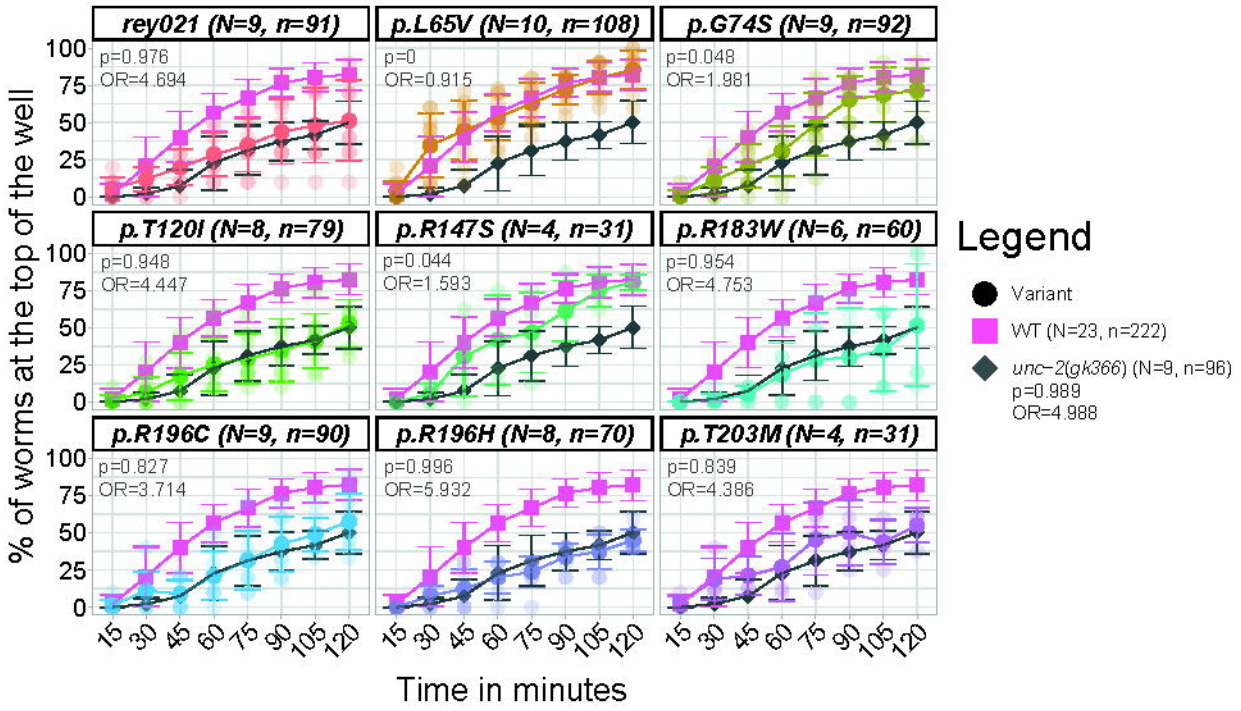

B

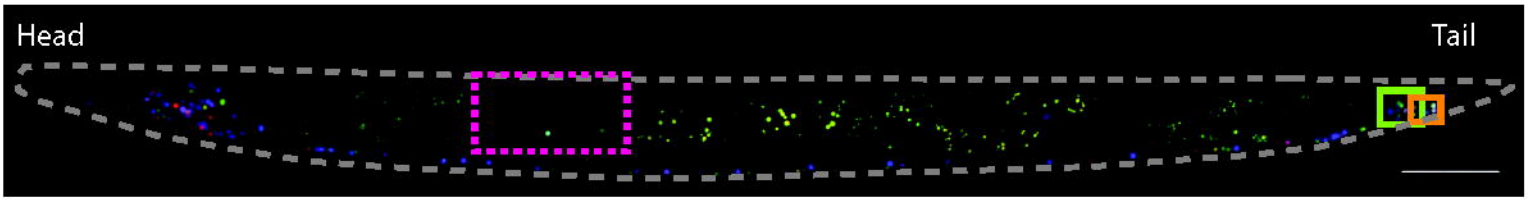

p.T120I

Additional neuronal cell (1/7)

p.R196C

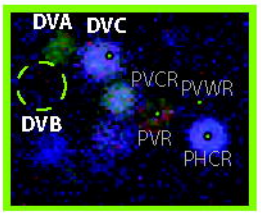

No DVB (1/15)

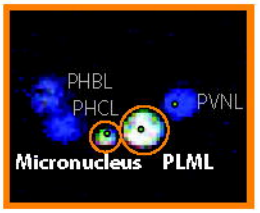

PLML micronucleus (1/15)

C

		L65V	G74S	T120I	R147S	R196C	R196H	T203M	rey021	WT
Additional Neuron	SDQR	0/8	0/7	1/7	0/8	1/6	0/3	0/9	1/6	0/5
	Other	1/14	1/14	0/16	0/14	0/15	0/15	1/12	1/15	0/14
Micronucleus		0/14	0/14	0/16	1/14	1/15	0/15	1/12	2/15	0/14
Missing Neuron	DVB	0/14	1/14	0/16	0/14	1/15	0/15	0/12	1/15	0/14
	PDA	0/14	1/14	0/16	0/14	0/15	0/15	0/12	0/15	0/14
	Other	0/14	1/14	3/16	1/14	0/15	0/15	2/12	2/15	0/14

Figure 5

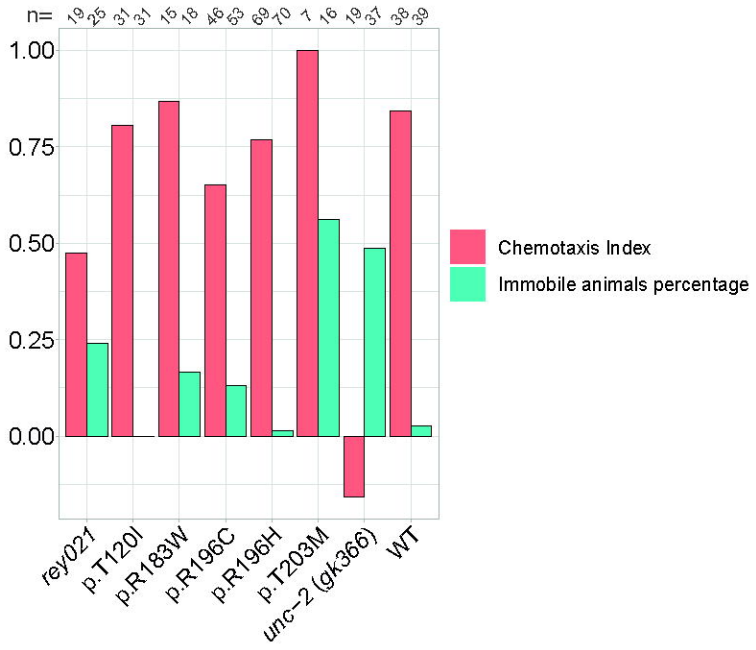
n=
19
25
31
31
15
18
46
53
69
70
7
16
19
37
38
39
1.00
0.75
0.50
0.25
0.00
rey021
p.T120I
p.R183W
p.R196C
p.R196H
p.T203M
unc-2 (gk366)
WT
Chemotaxis Index
Immobile animals percentage

Figure S5

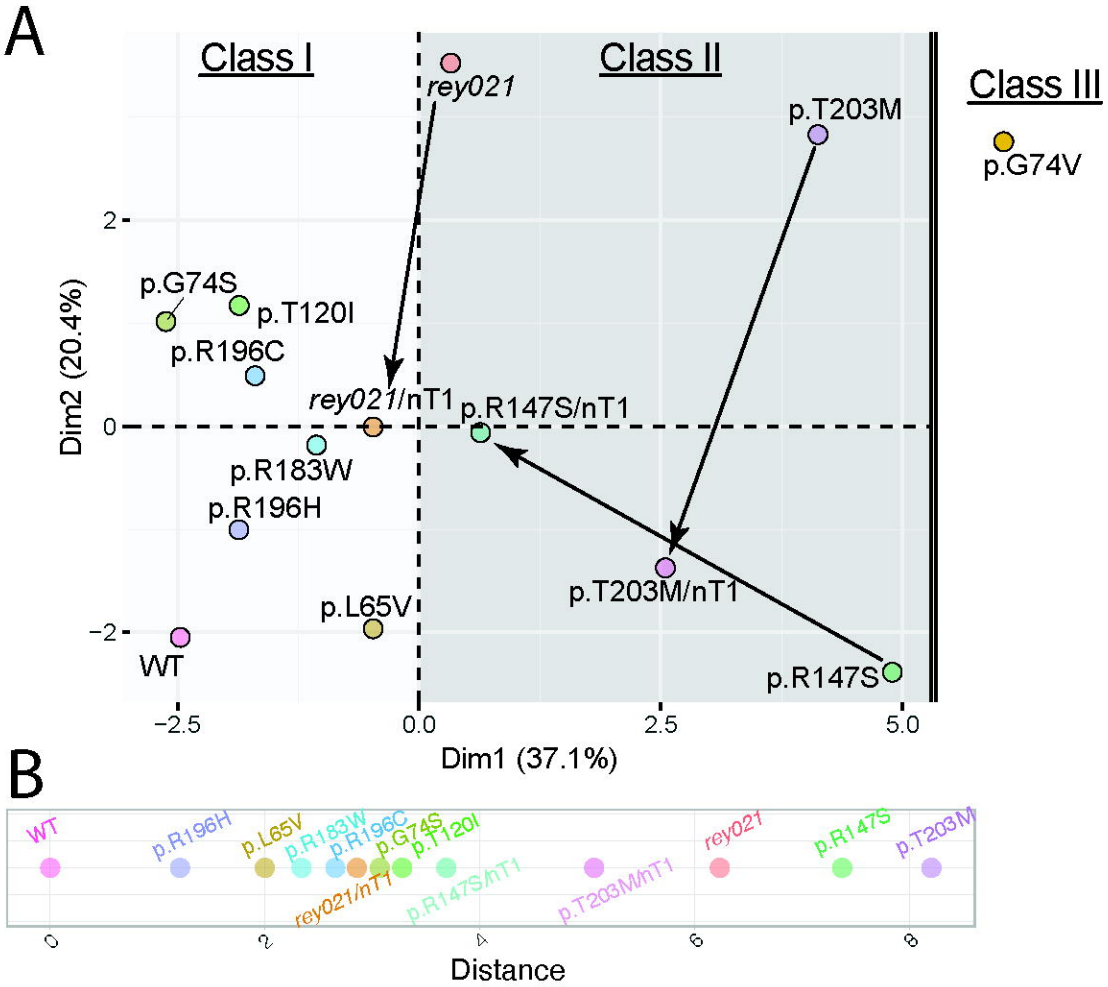
A
Class I
Class II
Class III
rey021
p.T203M
p.G74V
p.G74S
p.T120I
p.R196C
rey021/nT1
p.R147S/nT1
p.R183W
p.R196H
p.T203M/nT1
p.L65V
WT
p.R147S
Dim2 (20.4%)
Dim1 (37.1%)
2
0
−2
−2.5
0.0
2.5
5.0
B
WT
p.R196H
p.L65V
p.R183W
p.R196C
p.G74S
p.T120I
rey021/nT1
p.R147S/nT1
p.T203M/nT1
rey021
p.R147S
p.T203M
0
2
4
6
8
Distance

Figure 6

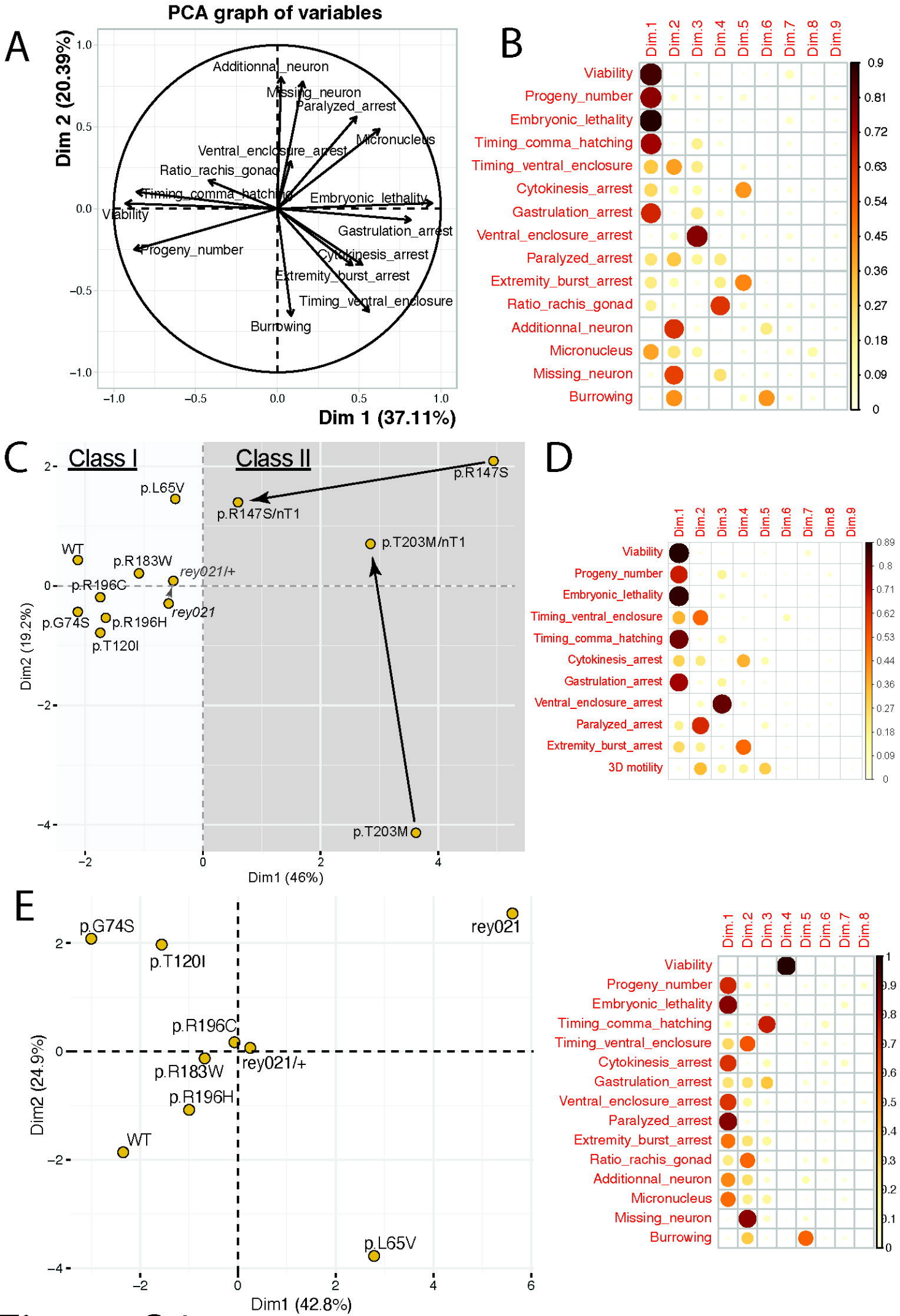
A
PCA graph of variables
Dim 1 (37.11%)
Dim 2 (20.39%)
Additionnal_neuron
Missing_neuron
Paralyzed_arrest
Micronucleus
Ventral_enclosure_arrest
Ratio_rachis_gonad
Timing_comma_hatching
Embryonic_lethality
Viability
Gastrulation_arrest
Progeny_number
Cytokinesis_arrest
Extremity_burst_arrest
Timing_ventral_enclosure
Burrowing
B
Dim.1
Dim.2
Dim.3
Dim.4
Dim.5
Dim.6
Dim.7
Dim.8
Dim.9
Viability
Progeny_number
Embryonic_lethality
Timing_comma_hatching
Timing_ventral_enclosure
Cytokinesis_arrest
Gastrulation_arrest
Ventral_enclosure_arrest
Paralyzed_arrest
Extremity_burst_arrest
Ratio_rachis_gonad
Additionnal_neuron
Micronucleus
Missing_neuron
Burrowing
C
Class I
Class II
p.L65V
p.R147S
p.R147S/nT1
p.T203M/nT1
WT
p.R183W
rey021/+
p.R196C
rey021
p.G74S
p.R196H
p.T120I
p.T203M
Dim2 (19.2%)
Dim1 (46%)
D
Viability
Progeny_number
Embryonic_lethality
Timing_ventral_enclosure
Timing_comma_hatching
Cytokinesis_arrest
Gastrulation_arrest
Ventral_enclosure_arrest
Paralyzed_arrest
Extremity_burst_arrest
3D motility
E
p.G74S
p.T120I
rey021
p.R196C
rey021/+
p.R183W
p.R196H
WT
p.L65V
Dim2 (24.9%)
Dim1 (42.8%)
Viability
Progeny_number
Embryonic_lethality
Timing_comma_hatching
Timing_ventral_enclosure
Cytokinesis_arrest
Gastrulation_arrest
Ventral_enclosure_arrest
Paralyzed_arrest
Extremity_burst_arrest
Ratio_rachis_gonad
Additionnal_neuron
Micronucleus
Missing_neuron
Burrowing

Figure S6